ATG9A protects plasma membrane from programmed and incidental permeabilization

Aurore Claude-Taupin[1,2], Jingyue Jia[1,2], Zambarlal Bhujabal[3], Meriem Garfa-Traoré[4], Suresh Kumar[1,2], Gustavo Peixoto Duarte da Silva[1,2,5], Ruheena Javed[1,2], Yuexi Gu[1,2], Lee Allers[1,2], Ryan Peters [1,2], Fulong Wang[1,2], Luciana Jesus da Costa[5], Sandeep Pallikkuth[6], Keith A. Lidke[6], Mario Mauthe[7], Pauline Verlhac[7], Yasuo Uchiyama[8], Michelle Salemi[9], Brett Phinney[9], Sharon A. Tooze[10], Muriel C. Mari[7], Terje Johansen[3], Fulvio Reggiori[7], and Vojo Deretic[1,2]*

[1]Autophagy, Inflammation and Metabolic (AIM) Center of Biochemical Research Excellence, University of New Mexico Health Sciences Center, 915 Camino de Salud, NE, Albuquerque, NM 87131, USA.
[2]Department of Molecular Genetics and Microbiology, University of New Mexico Health Sciences Center, 915 Camino de Salud, NE, Albuquerque, NM 87131, USA.
[3]Molecular Cancer Research Group, Institute of Medical Biology, University of Tromsø– The Arctic University of Norway, 9037 Tromsø,Norway
[4]Cell Imaging Platform, INSERM US24 Structure Fédérative de Recherche Necker, Université de Paris, Paris, France.
[5]Departamento de Virologia, Instituto de Microbiologia Paulo de Góes, Universidade Federal do Rio de Janeiro, Rio de Janeiro, Brazil.
[6]Department of Physics and Astronomy, University of New Mexico, Albuquerque, NM 87131, USA.
[7]Department of Biomedical Sciences of Cells & Systems, University of Groningen, University Medical Center Groningen, Groningen, The Netherlands.
[8]Department of Cellular and Molecular Neuropathology; Juntendo University Graduate School of Medicine; Bunkyo-Ku, Tokyo 113--8421, Japan
[9]Proteomics Core Facility, UC Davis Genome Center, University of California, Davis, CA 95616, USA
[10]The Francis Crick Institute, Molecular Cell Biology of Autophagy Laboratory, 1 Midland Road, London NW1 1AT, UK.

*Correspondence:
Vojo Deretic, Ph.D.
University of New Mexico Health Sciences Center
915 Camino de Salud, NE
Albuquerque, NM 87131
U.S.A.
(505) 272-3814
vderetic@salud.unm.edu

The integral membrane protein ATG9A plays a key role in autophagy. It displays a broad intracellular distribution and is present in numerous compartments including the plasma membrane (PM). The reasons for ATG9A's distribution to the PM and its role at the PM are not understood. Here we show that ATG9A organizes, in concert with IQGAP1, components of the ESCRT system and uncover cooperation between ATG9A, IQGAP1 and ESCRTs in protection against PM damage. ESCRTs and ATG9A phenocopied each other in protection against PM injury. ATG9A knockouts sensitized PM to permeabilization by a broad spectrum of microbial and endogenous agents including gasdermin, MLKL, and MLKL-like action of coronavirus ORF3a. Thus, ATG9A engages IQGAP1 and the ESCRT system to maintain PM integrity.

Introduction

The autophagy[1, 2] and ESCRT systems[3-5] both act in the remodeling of cellular membranes and contribute to a range of intracellular homeostatic functions and biological processes. The classical panel of ESCRT activities is diverse[3-5] and affects many organelles and functions including plasma membrane (PM) repair[6-9]. Autophagy in turn, along with its variations[10], contributes to a range of intracellular homeostatic activities[11] and is impaired in medical conditions[2] that often have strong inflammatory components[12].

The canonical autophagy pathway turns over defective and surplus cytoplasmic components and contributes to protein and organellar quality control[1]. It also has a parallel, purely metabolic function[13]. The mammalian autophagy pathway depends on ATG factors organized in a network of protein modules[1], extensive lipid transactions[14-17], and protein-lipid and protein-protein interactions within the modules and between the modules[1]. When autophagy is set in motion, the modules interlock[1]. After initiation and subsequent stages, degradative autophagy terminates in the formation of autolysosomes[18].

Until very recently[16, 17, 19], the core mammalian autophagy factor ATG9A has been less understood. The elucidation of high-resolution cryo-EM structure and functional studies have revealed that both yeast Atg9 and mammalian ATG9A are lipid scramblases that play a role in autophagosome expansion[16, 17, 19], consistent with the yeast Atg9 localizing at the tips of a growing phagophore[20], where it also organizes several components of the Atg machinery, including Atg2[20]. However, mammalian ATG9A is present in numerous intracellular compartments, including TGN, early and recycling endosomes[21, 22], and traffics through the secretory pathway to the PM and to the endocytic pathway from the PM[23, 24]. The complex intracellular localization and trafficking of ATG9A in mammalian cells suggests existence of additional functions of ATG9A that are yet to be defined.

Here we report a novel function of ATG9A associated with its trafficking through the PM. ATG9A protects cells from PM damage caused by a spectrum of exogenous and endogenous agents including permeabilization by gasdermin and MLKL, which generate pores at the PM[25] or perturb PM integrity[26, 27], respectively, during programmed cell death processes of pyroptosis[28, 29] and necroptosis[30, 31]. We furthermore define a new ATG9A-IQGAP1 apparatus that integrates with the ESCRT system[3-5] to cooperatively heal areas of PM damage.

Results

ATG9A protects cells against plasma membrane damage

We hypothesized that ATG9A, which traffics through numerous membranous compartments[21, 23, 32-34], functions in membrane damage homeostasis. Due to its presence on plasma membrane (PM)[23, 24, 35], we tested its role in protection against PM injury. A propidium iodide (PI) uptake assay[6] was adapted for PM damage quantification by high content microscopy (HCM) of adherent cells (Fig. 1a). Knocking out *ATG9A* in Huh7 cells (ATG9A$^{Huh7\text{-}KO}$) (Fig. 1b) rendered them more susceptible to injury by digitonin, saponin or streptolysin O (SLO) (Fig. 1c-d, Extended Data Fig. 1a). Transfection with GFP-ATG9A or FLAG-ATG9A rescued ATG9A$^{Huh7\text{-}KO}$ cells (Extended Data Fig. 1b,c).

We employed additional methods and developed an assay (PMHAL) to quantify PM damage based on a HaloTag probe (GFP-HT) and membrane permeant and impermeant fluorescent chloroalkane ligands (MPL and MIL; Fig. 1e). In damaged cells, GFP-HT labels with both ligands whereas in undamaged cells it labels only with MPL. Untreated ATG9A$^{Huh7\text{-}KO}$ and ATG9A$^{Huh7\text{-}WT}$ cells expressing GFP-HT stained with MPL, whereas when treated with digitonin ATG9A$^{Huh7\text{-}WT}$ cells stained weakly and ATG9A $^{Huh7\text{-}KO}$ cells stained strongly with MIL (Fig. 1f-g, Extended Data Fig. 1d-f). Using Dextran-10k (Dx-10) as another probe for PM permeability, we observed increased staining in ATG9A$^{Huh7\text{-}KO}$ relative to ATG9A$^{Huh7\text{-}WT}$ cells (Extended Data Fig. 1g). Changes in endocytosis did not cause these differences, as ATG9A$^{Huh7\text{-}KO}$ and ATG9A$^{Huh7\text{-}WT}$ cells internalized equally the endocytic probe DQ-Red-BSA (Extended Data Fig. 1h). Endosomal multivesicular body (MVB) biogenesis was not altered in ATG9A$^{Huh7\text{-}KO}$ cells, quantified by lysobisphosphatidic acid (LBPA) staining visualized in enlarged vesicles induced by Rab5^{Q79L} (Extended Data Fig. 1i,j). Plasma membrane tension, a measure of PM lipid ordering[36] was not altered in ATG9A$^{Huh7\text{-}KO}$ relative to ATG9A$^{Huh7\text{-}WT}$ cells (Extended Data Fig. 1k,l), based on equal fluorescence lifetimes of Flipper-TR®, a membrane tension probe[36]. In the absence of extracellular Ca^{2+}, both ATG9A$^{Huh7\text{-}KO}$ and ATG9A$^{Huh7\text{-}WT}$ cells showed equal levels of PM damage, whereas with the added free Ca^{2+} during digitonin exposure, ATG9A$^{Huh7\text{-}KO}$ cells experienced relatively more damage

compared to the ATG9A$^{Huh7\text{-}WT}$ cells (Figure 1h, Extended Data Fig. 1m). Thus, ATG9A protects cells from PM damage through an active, Ca^{2+}-dependent, process elicited upon damage rather than by passively affecting PM sensitivity to damaging agents.

Additional cell types were tested. Increased sensitivity to digitonin-caused PM damage was observed in ATG9A$^{MCF7\text{-}KO}$ vs. parental ATG9A$^{MCF7\text{-}WT}$ cells and in HeLa cells knocked-down for ATG9A (Extended Data Fig. 1n-u). We tested primary cells using murine bone marrow-derived macrophages (BMMs). BMMs from Atg9a$^{fl/fl}$ LysM-Cre^{+} mice were also more sensitive to PM damage caused by digitonin or SLO relative to BMMs from Atg9a$^{fl/fl}$ LysM-Cre^{-} mice (Extended Data Fig. 2a-d). In summary, ATG9A protects cells from PM damage (Fig. 1i).

ATG9A protects plasma membrane against gasdermin pores

We tested the role of ATG9A in protection against PM permeabilization in the context of a known physiological process. During pyroptosis, gasdermin pores form on the PM after proteolytic processing of gasdermin-D (GSDMD) entailing liberation of the N-terminal fragment (GSDMD-NT) and its subsequent oligomerization into a pore-like structure at the PM[37]. Overexpressing GSDMD-NT increased PI uptake more in Huh7 ATG9A^{KO} than in parental ATG9A^{WT} Huh7 cells (Fig. 2a), paralleled by reduced staining with calcein, a cell viability reporter (Fig. 2a, inset and Extended Data Fig. 2e). We next tested effects of ATG9A on PM permeabilization upon activation of endogenous GSDMD by electroporated or transfected LPS into U2OS and BMMs. Processing of endogenous GSDMD monitored by GSDMD-NT release was equal in LPS-electroporated ATG9A$^{U2OS\text{-}KO}$ vs. ATG9A$^{U2OS\text{-}WT}$ cells and in LPS-primed and then LPS-transfected Atg9a$^{fl/fl}$ LysM-Cre^{+} BMMs vs. Atg9a$^{fl/fl}$ LysM-Cre^{-} BMMs (Fig. 2b,c). In each case, ATG9A^{KO} cells were more susceptible than ATG9A^{WT} cells to activated endogenous gasdermin in a time- and dose-dependent manner (Fig. 2d-g). Thus, ATG9A protects cells against PM permeabilization caused by gasdermin pores (Fig. 2h).

ATG9A translocation to PM protects cells from damage

At least a fraction of ATG9A undergoes vesicular trafficking to and from the PM[23, 24, 35]. Using MyrPalm-EGFP as a PM marker[6], increased presence of ATG9A was detected at the PM following damage with digitonin, SLO, saponin, or by glass bead-inflicted injury (GBI) (Fig. 3a,b and Extended Data Fig. 3a). TIRF super-resolution microscopy confirmed ATG9A's appearance at the PM after injury (Fig. 3c and Extended Data Fig. 3b) further biochemically ascertained by surface biotinylation[38] (Extended Data Fig. 3c). ATG9A translocation to PM and PM protection against damage were sensitive to N-ethylmaleimide (NEM), an antagonist of SNARE-based membrane fusion (Extended Data Fig. 3d-g).

We carried out ultrastructural analysis by electron microscopy (EM) using APEX2 as an EM tag. A Flp-In Tet^{ON} FLAG-APEX2-ATG9A cell line (HEK293T$^{APEX2\text{-}ATG9A}$, Extended Data Fig. 3h) showed increased diaminobenzidine precipitates at the PM when cells were subjected to PM damage (Fig. 3d,e and Extended Data Fig. 3i-n). Thus, ATG9A translocates to PM upon its damage (Extended Data Fig. 3o).

The Y8F mutation retards ATG9A removal from PM during its trafficking[24]. Expression of FLAG-ATG9A^{Y8F} partially protected cells against PM damage (Fig. 3f,g and Extended Data Fig. 4a). Physiological enhancement of ATG9A's presence at the PM in cells pulsed with EGF[24]-increased protection against PM damage, an effect abrogated in ATG9A$^{Huh7\text{-}KO}$ cells" (Extended Data Fig. 4b-d). Thus, ATG9A's presence at the PM confers protection against PM injury (Extended Data Fig. 4e,f).

ATG9A's partner IQGAP1 confers protection against PM damage

Proteomics of ATG9A-containing membranes have been reported[32, 39]. Here, we identified specific interactors of ATG9A during PM damage using APEX2-ATG9A as a tool for proximity biotinylation of closely apposed partners[40]. APEX2-ATG9A construct was compatible with known functions of ATG9A, i.e. APEX2-ATG9A rescued the LC3 lipidation defect in ATG9A$^{Huh7\text{-}KO}$ cells under autophagy-inducing conditions (Extended Data Fig. 5a). The HEK293T$^{APEX2\text{-}ATG9A}$ cells (Extended Data Figs. 3h and 5b), were treated with digitonin, SLO or GBI followed by APEX2 biotinylation reaction [40, 41] and

ATG9A partners identified through LC-MS/MS analysis of the biotinylated proteins (Supplementary Table 1, Fig. 4a, and Extended Data Fig. 5c-f).

Among newly identified ATG9A interactors were IQGAPs[42], with IQGAP1 showing the highest number of peptides and dynamic changes during PM damage (Fig. 4a, Extended Data Fig. 5c,d and Supplementary Table 1, Tabs 1, 3, 5). The increased IQGAP1-ATG9A association during PM damage was confirmed by co-immunoprecipitation experiments (co-IPs) (Fig. 4b, Extended Data Fig. 6a). FLAG-ATG9A and IQGAP1 colocalized at the PM upon treatment with digitonin (Extended Data Fig. 6b,c). ATG9A and IQGAP1 directly interact, as established in GST pulldowns (Fig. 4c). In these experiments, GST fusion with full size ATG9A could not be efficiently expressed, but a GST-ATG9A lacking the last 255 residues of its long C-terminal domain was stable and bound IQGAP1. Recent cryo-EM structures of human ATG9A have revealed the organization of complex cytosolic domains[16, 17, 19]. When we tested cytosolic domains individually, which are adjacent in the 3D CryoEM structure of ATG9A, they showed capacity to associate with IQGAP1 in GST pulldowns (Extended Data Fig. 6d-f).

IQGAP1 knockdown (Extended Data Fig. 6g) increased PI uptake (Fig. 4d) and prevented ATG9A translocation to PM upon injury (Extended Data Fig. 6h). Thus, IQGAP1 controls ATG9A recruitment to PM during damage. As with ATG9A, IQGAP1 knockdown did not reduce MVB levels quantified by LBPA staining (Extended Data Fig. 6i,j). IQGAP1 responds to Ca^{2+} fluxes[42] and the role of ATG9A protection against PM damage depended on extracellular Ca^{2+} (Fig. 1h). In the absence of Ca^{2+}, ATG9A translocation to injured PM and co-IP between ATG9A and IQGAP1 were lost (Extended Data Fig. 6k-n). Thus, Ca^{2+}, IQGAP1 and ATG9A together confer protection against PM damage (Fig. 4e).

ATG9A interacts with ESCRTs

Proximity biotinylation proteomic analyses uncovered ESCRTs as partners of ATG9A (Supplementary Table 1, Tabs 1,3,5,8,10). Proteins from most ESCRT subcomplexes[3-5] were detected in ATG9A's proximity, including TSG101 and ALIX (PDCD6IP)

(Supplementary Table 1, Tabs 8,9,10). These data suggest a previously unappreciated property of ATG9A to associate with multiple ESCRT components. We confirmed ATG9A interactions with TSG101 and the ALIX V domain in co-IPs (Fig. 5a, Extended Data Fig. 6a and 7a,b). Interactions between APEX2-ATG9A and endogenous TSG101 and ALIX were additionally assessed in a modified proximity biotinylation assay, which consisted of affinity purification on avidin beads of APEX2 proximity-*bio*tinylated proteins and their detection by *We*stern *b*lotting (BioWeB assay; Fig. 5b). Using BioWeB, we observed in HEK293T$^{APEX2\text{-}ATG9A}$ cells subjected to PM damage, enrichment of endogenous TSG101 (Fig. 5c,d) but not of ALIX (Extended Data Fig. 7c) in the vicinity ATG9A. The TSG101 enrichment in co-IP and BioWeB assays with ATG9A, reflects at least in part increased association of IQGAP1 with ATG9A during PM damage (Extended Data Fig. 6a) and is in keeping with the reported binding of IQGAP1 to TSG101[43]. Consistent with this, IQGAP1 knockdown indicated a decrease of TSG101 in immunoprecipitates of endogenous ATG9A from cells subjected to PM damage injury (Extended Data Fig. 8a).

We tested whether ESCRT-III effector components acting downstream of TSG101 and ALIX[3] can be detected in protein complexes with ATG9A. FLAG-CHMP4A and Myc-CHMP4B were detected in co-IPs with GFP-ATG9A after PM damage (Fig. 5e,f). Using TIRF and quantifying CHMP4B profiles at the PM, their increase upon injury was sensitive to NEM (Fig. 5g,h and Extended Data Fig. 8b) paralleling sensitivity of ATG9A profiles (Extended Data Fig. 3d-f). Increases in both CHMP4A and CHMP4B profiles, detectable at the PM during damage, depended on Ca^{2+} and ATG9A, as visualized by confocal microscopy (Extended Data Fig. 8c,d), and quantified by TIRF microscopy and HCM (Fig. 5i-l). GFP-ATG9A and mCherry-CHMP4B appeared juxtaposed following GSDMD-NT-induced PM damage (Extended Data Fig. 8e). Thus, components of the ESCRT machinery associate with ATG9A, appear together on PM, and these relationships increase in response to PM damage.

ESCRTs and ATG9A cooperate in protection against PM damage

The ESCRT components play a role in protection against PM damage[6-9]. We tested whether ESCRTs participate in protection against PM injury conferred by ATG9A.

TSG101 knockdown increased sensitivity to PM damage by digitonin whereas ALIX knockdown did not, and combined knockdown of ALIX and TSG101 showed no increase in damage relative to single knockdown of TSG101 (Fig. 6a-c). A CRISPR knockout of ALIX did not increase susceptibility to digitonin injury (Fig. 6a-c). Prior publications have indicated that ALIX does not contribute to protection against certain types of PM permeabilization, such as those caused by effectors of necroptosis and pyroptosis[8, 9]. We could not test overlapping/additive effects of ATG9A and TSG101 because we observed that TSG101 was destabilized in ATG9A^{KO} cells and in cells subjected to ATG9A knockdowns. We nevertheless tested contributions of CHMP2A, which is a key downstream ESCRT-III factor that is often used to establish the role of ESCRT-dependent membrane remodeling in different cellular processes[6, 9, 44]. Knocking down CHMP2A increased sensitivity of ATG9A$^{Huh7\text{-}WT}$ but not of ATG9A$^{Huh7\text{-}KO}$ cells to digitonin or GSDMD (Fig. 6d-g). Moreover, CHMP2A directly binds IQGAP1 (GST-pulldowns; Fig 6h,i). Thus, ATG9A, IQGAP1 and ESCRTs are components of the same pathway protecting cells from PM damage (Fig. 6j).

Contributions of other ATG9A partners and ATG9A functions

In addition to ESCRTs and IQGAPs, our proximity biotinylation proteomic analyses revealed additional ATG9A interactors, such as Rab GTPases and adaptor proteins (Supplementary Table 1, Tabs 7 and 8), as well as several ATG proteins (Supplementary Table 1, Tab10).

ATG2A and B have been perceived as ATG9A interactors, as in yeast[20], and act in lipid transport[14]. We detected ATG2 peptides with APEX2-ATG9A (Supplementary Table 1, Tab10). When ATG2A or ATG2B were knocked out by CRISPR, this did not affect sensitivity to digitonin or endogenous gasdermin activation (Extended Data Fig. 9a-e). Downregulating another lipid-modifying factor found on ATG9A membranes, PI4KB[39], did not affect PM damage (Extended Data Fig. 9f,g). A lipid scramblase activity has been recently reported for ATG9A[16, 17]. We tested whether the ATG9A mutant M33 (autophagy-defective and scramblase-defective; K321L, R322L, E323L, T419W)[17] lost the ability to protect PM from damage. However, ATG9A-M33 complemented ATG9A$^{Huh7\text{-}KO}$ cells in

the digitonin PM-damage test (Extended Data Fig. 9h). Thus, ATG9A's activities defective in the M33 mutant[17] do not appear to be essential for protection against PM damage.

Additional ATG9A partners observed in proximity biotinylation proteomic analyses were confirmed for interactions with ATG9A and some were tested for effects on PM sensitivity to damage (Extended Data Fig. 9i-q).

ATG9A affects membrane dynamics and shedding

PM repair is often accompanied by membrane rearrangements and emission of membranous particles[6, 7, 45]. Localized laser-induced PM injury, albeit different from other non-confined types of PM damage in this work, was employed for live microscopy observations. GFP-ATG9A coalesced at the interface between the cytosol and protruding membranes that became diffusionally separated (Supplementary Video 1, Extended Data Fig. 10a). Following PM damage with digitonin, particles were released that showed a relatively homogenous peak at 95 nm in ATG9A$^{Huh7\text{-}WT}$, which shifted to smaller sizes in ATG9A$^{Huh7\text{-}KO}$ cells (75 nm, Fig. 7a,b and Extended Data Fig. 10b,c). The particles released by ATG9A$^{Huh7\text{-}KO}$ were enriched for the membrane marker CD63 relative to the particles released from ATG9A$^{Huh7\text{-}WT}$ (Extended Data Fig. 10d). Thus, ATG9A participates in dynamic events at the PM and affects the size and type of membranous particles emitted during PM damage.

ATG9A protects PM from damage by diverse biological agents

Our findings that ATG9A protects against endogenous PM-permeabilizing agents such as GSDMD-NT (Fig. 2) correlate with the reports that the ESCRT system protects cells during gasdermin-mediated pyroptotic cell death[8]. Another cell death process, necroptosis, is associated with mixed lineage kinase domain like (MLKL)-dependent loss of PM integrity and it too is countered by ESCRT-III[9]. We expressed the characterized PM-targeting MLKL system (full length MLKL-Venus tagged with HRas$_{25}$ PM-targeting motif) sufficient to cause a loss of PM integrity[27], and detected increased PM permeability in ATG9A$^{Huh7\text{-}KO}$ compared to ATG9A$^{Huh7\text{-}WT}$ cells (Fig. 7c). Moreover, ATG9A protected cells against PM leakage caused by SARS-CoV-2 ORF3a, an activity previously reported

for SARS-CoV-1[46] (Fig. 7d). In complementation experiments, ATG9A WT rescued ATG9A$^{Huh7\text{-}KO}$ cells subjected to SARS-CoV-2 ORF3a-induced PM damage (Fig. 7e). Mirroring results in complementation experiments with digitonin treatment, ATG9A-M33 rescued ATG9A$^{Huh7\text{-}KO}$ cells damaged by SARS-CoV-2 ORF3a (Fig. 7e). In conclusion, ATG9A counters physiological PM perturbations associated with pyroptotic and necroptotic programmed cell death pathways.

External biological agents, such as infectious agents, including bacteria, viruses and protozoan parasites, can cause host cell membrane damage. The intracellular pathogen *Mycobacterium tuberculosis* (*Mtb*) causes partial phagosomal permeabilization whereas a subset of autophagy factors plays a role in controlling Mtb infection[47, 48]. However, *Mtb* also causes PM damage while interacting with host cells[49, 50]. We thus tested whether ATG9A can protect cells from PM damage caused by *Mtb*. To avoid complications from intracellular *Mtb* effects, we used nonphagocytic Huh7 cells, exposed them to virulent *Mtb*, and quantified PI staining, which showed increased *Mtb*-inflicted PM damage in the absence of ATG9A (Fig. 7f and Extended Data Fig. 10e). As a control, we used nonvirulent derivative of *Mtb* subspecies bovis (BCG) and detected neither PM damage nor increase dependent on ATG9A (Extended Data Fig. 10f,g). Thus, ATG9A plays a protective role against PM damage caused by *Mtb*.

Discussion

In this study, we have uncovered a hitherto unknown role of ATG9A in PM repair. In response to Ca^{2+} influx due to PM damage, IQGAP1, ATG9A and ESCRTs are recruited to the sites of injury for repair (Fig. 7g). IQGAP1, a known Ca^{2+} responder[42], recruits ATG9A to damaged PM, and together they organize ESCRT machinery for PM repair. ATG9A has been traditionally viewed as an important autophagy factor, whereas based on our results it should also be considered as a peripheral factor cooperating with the ESCRT system. ATG9A and IQGAP1 combine with its ESCRT effectors in protection against GSDMD and MLKL pores [8, 9] to prevent excessive necrotic death. This may be of significance in controlling inflammation and tissue damage under various pathophysiological conditions.

Our MS analyses uncovered the hitherto unknown association of ATG9A with IQGAPs, a class of proteins that along with their binding partner calmodulin act as Ca^{2+}-sensing factors[51-55], with IQGAP1 better known for their ability to govern cytoskeletal rearrangements at the leading edge of the PM in migrating cells[56, 57]. ATG9A-IQGAP1 interactions defined here and the previously known functions of IQGAP1 are furthermore compatible with the reported role of ATG9A in cell migration[58]. Others have described a process where Ca^{2+} recruits ALG-2 and ESCRTs to repair PM upon laser-induced PM damage[7]. However, ALG-2 does not play a role in protection against GSDMD or MLKL-induced PM damage[8, 9].

In addition to ESCRT components, our proteomic findings include a variety of previously reported ATG9A partners identified by conventional biochemical methods, validating the use of APEX2-ATG9A. The repertoire of ATG9A interactors includes a suite of Rab GTPases, likely reflecting the multiple trafficking routes taken by ATG9A. This may include the small vesicles observed subcortically during PM damage, that we propose ferry ATG9A en route to or from PM. The Rab GTPases identified in the proximity of ATG9A include RAB7A, which is known to colocalize with ATG9A[21], and a RAB7-specific GTPase activating protein (GAP), TBC1D15[59], underscoring the role of RAB7 in ATG9A

trafficking that is also reflected in observed sensitivity of RAB7-depleted cells to PM damage. By MS, we also detected dynamic changes in associations and confirmed several by co-IPs with the adaptor proteins, AP-1, AP-2, AP-3 (AP3 interaction being identified here), and AP-4[24, 35, 60]. We interpret these relationships as indicative of increased ATG9A trafficking during PM damage.

Our findings suggest that ATG9A confers protection against diverse PM-damaging products and activities, including those of microbial pathogens. ATG9A protects cells from PM injury caused by *M. tuberculosis*[49, 50, 61]. Likewise, SARS-CoV-1 ORF3a[46] and, as shown here, ORF3a of SARS-CoV-2 cause PM damage and ATG9A protects against that activity. ORF3a, apart from its membrane permeabilization activities also plays a role in lysosomal damage/deacidification with a proposed contribution to nonlytic viral egress via endosomal/lysosomal exocytosis[62]. Thus, ATG9A activities at the PM intersect with a spectrum of microbial pathogenesis processes. This is in keeping with a growing recognition of the expanding effects of the components of the autophagy apparatus in various cellular processes[2, 10]. The physical and functional cooperation of ATG9A with IQGAP1 and ESCRT machinery represents another example of non-canonical functions of the ATG factors and broadens the fundamental scope and translational potential of both the ATG and the ESCRT systems.

References

1. Morishita, H. & Mizushima, N. Diverse Cellular Roles of Autophagy. *Annu Rev Cell Dev Biol* **35**, 453-475 (2019).
2. Levine, B. & Kroemer, G. Biological Functions of Autophagy Genes: A Disease Perspective. *Cell* **176**, 11-42 (2019).
3. Christ, L., Raiborg, C., Wenzel, E.M., Campsteijn, C. & Stenmark, H. Cellular Functions and Molecular Mechanisms of the ESCRT Membrane-Scission Machinery. *Trends Biochem Sci* **42**, 42-56 (2017).
4. Hurley, J.H. ESCRTs are everywhere. *EMBO J* **34**, 2398-2407 (2015).
5. Gatta, A.T. & Carlton, J.G. The ESCRT-machinery: closing holes and expanding roles. *Curr Opin Cell Biol* **59**, 121-132 (2019).
6. Jimenez, A.J. *et al.* ESCRT machinery is required for plasma membrane repair. *Science* **343**, 1247136 (2014).
7. Scheffer, L.L. *et al.* Mechanism of Ca(2)(+)-triggered ESCRT assembly and regulation of cell membrane repair. *Nat Commun* **5**, 5646 (2014).

8. Ruhl, S. *et al.* ESCRT-dependent membrane repair negatively regulates pyroptosis downstream of GSDMD activation. *Science* **362**, 956-960 (2018).
9. Gong, Y.N. *et al.* ESCRT-III Acts Downstream of MLKL to Regulate Necroptotic Cell Death and Its Consequences. *Cell* **169**, 286-300 e216 (2017).
10. Galluzzi, L. & Green, D.R. Autophagy-Independent Functions of the Autophagy Machinery. *Cell* **177**, 1682-1699 (2019).
11. Mizushima, N. & Levine, B. Autophagy in Human Diseases. *N Engl J Med* **383**, 1564-1576 (2020).
12. Deretic, V. Autophagy in inflammation, infection, and immunometabolism. *Immunity* **54**, 437-453 (2021).
13. Lahiri, V., Hawkins, W.D. & Klionsky, D.J. Watch What You (Self-) Eat: Autophagic Mechanisms that Modulate Metabolism. *Cell Metab* **29**, 803-826 (2019).
14. Valverde, D.P. *et al.* ATG2 transports lipids to promote autophagosome biogenesis. *J Cell Biol* **218**, 1787-1798 (2019).
15. Maeda, S., Otomo, C. & Otomo, T. The autophagic membrane tether ATG2A transfers lipids between membranes. *Elife* **8** (2019).
16. Matoba, K. *et al.* Atg9 is a lipid scramblase that mediates autophagosomal membrane expansion. *Nat Struct Mol Biol* **27**, 1185-1193 (2020).
17. Maeda, S. *et al.* Structure, lipid scrambling activity and role in autophagosome formation of ATG9A. *Nat Struct Mol Biol* **27**, 1194-1201 (2020).
18. Zhao, Y.G. & Zhang, H. Autophagosome maturation: An epic journey from the ER to lysosomes. *J Cell Biol* **218**, 757-770 (2019).
19. Guardia, C.M. *et al.* Structure of Human ATG9A, the Only Transmembrane Protein of the Core Autophagy Machinery. *Cell Rep* **31**, 107837 (2020).
20. Gomez-Sanchez, R. *et al.* Atg9 establishes Atg2-dependent contact sites between the endoplasmic reticulum and phagophores. *J Cell Biol* **217**, 2743-2763 (2018).
21. Young, A.R. *et al.* Starvation and ULK1-dependent cycling of mammalian Atg9 between the TGN and endosomes. *J Cell Sci* **119**, 3888-3900 (2006).
22. Longatti, A. *et al.* TBC1D14 regulates autophagosome formation via Rab11- and ULK1-positive recycling endosomes. *J Cell Biol* **197**, 659-675 (2012).
23. Puri, C., Renna, M., Bento, C.F., Moreau, K. & Rubinsztein, D.C. Diverse autophagosome membrane sources coalesce in recycling endosomes. *Cell* **154**, 1285-1299 (2013).
24. Zhou, C. *et al.* Regulation of mATG9 trafficking by Src- and ULK1-mediated phosphorylation in basal and starvation-induced autophagy. *Cell Res* **27**, 184-201 (2017).
25. Broz, P., Pelegrin, P. & Shao, F. The gasdermins, a protein family executing cell death and inflammation. *Nat Rev Immunol* **20**, 143-157 (2020).
26. Wang, H. *et al.* Mixed lineage kinase domain-like protein MLKL causes necrotic membrane disruption upon phosphorylation by RIP3. *Mol Cell* **54**, 133-146 (2014).
27. Quarato, G. *et al.* Sequential Engagement of Distinct MLKL Phosphatidylinositol-Binding Sites Executes Necroptosis. *Mol Cell* **61**, 589-601 (2016).
28. Kayagaki, N. *et al.* Caspase-11 cleaves gasdermin D for non-canonical inflammasome signalling. *Nature* **526**, 666-671 (2015).
29. Shi, J. *et al.* Cleavage of GSDMD by inflammatory caspases determines pyroptotic cell death. *Nature* **526**, 660-665 (2015).

30. Pasparakis, M. & Vandenabeele, P. Necroptosis and its role in inflammation. *Nature* **517**, 311-320 (2015).
31. Weinlich, R., Oberst, A., Beere, H.M. & Green, D.R. Necroptosis in development, inflammation and disease. *Nat Rev Mol Cell Biol* **18**, 127-136 (2017).
32. Kakuta, S. *et al.* Small GTPase Rab1B is associated with ATG9A vesicles and regulates autophagosome formation. *FASEB J* **31**, 3757-3773 (2017).
33. Karanasios, E. *et al.* Autophagy initiation by ULK complex assembly on ER tubulovesicular regions marked by ATG9 vesicles. *Nat Commun* **7**, 12420 (2016).
34. Orsi, A. *et al.* Dynamic and transient interactions of Atg9 with autophagosomes, but not membrane integration, are required for autophagy. *Mol Biol Cell* **23**, 1860-1873 (2012).
35. Popovic, D. & Dikic, I. TBC1D5 and the AP2 complex regulate ATG9 trafficking and initiation of autophagy. *EMBO Rep* **15**, 392-401 (2014).
36. Colom, A. *et al.* A fluorescent membrane tension probe. *Nat Chem* **10**, 1118-1125 (2018).
37. Ding, J. *et al.* Pore-forming activity and structural autoinhibition of the gasdermin family. *Nature* **535**, 111-116 (2016).
38. Mellgren, R.L. A new twist on plasma membrane repair. *Commun Integr Biol* **4**, 198-200 (2011).
39. Judith, D. *et al.* ATG9A shapes the forming autophagosome through Arfaptin 2 and phosphatidylinositol 4-kinase IIIbeta. *J Cell Biol* **218**, 1634-1652 (2019).
40. Lam, S.S. *et al.* Directed evolution of APEX2 for electron microscopy and proximity labeling. *Nat Methods* **12**, 51-54 (2015).
41. Jia, J. *et al.* Galectins Control mTOR in Response to Endomembrane Damage. *Mol Cell* **70**, 120-135 e128 (2018).
42. Hedman, A.C., Smith, J.M. & Sacks, D.B. The biology of IQGAP proteins: beyond the cytoskeleton. *EMBO Rep* **16**, 427-446 (2015).
43. Morita, E. *et al.* Human ESCRT and ALIX proteins interact with proteins of the midbody and function in cytokinesis. *EMBO J* **26**, 4215-4227 (2007).
44. Denais, C.M. *et al.* Nuclear envelope rupture and repair during cancer cell migration. *Science* **352**, 353-358 (2016).
45. Keyel, P.A. *et al.* Streptolysin O clearance through sequestration into blebs that bud passively from the plasma membrane. *J Cell Sci* **124**, 2414-2423 (2011).
46. Yue, Y. *et al.* SARS-Coronavirus Open Reading Frame-3a drives multimodal necrotic cell death. *Cell Death Dis* **9**, 904 (2018).
47. Gutierrez, M.G. *et al.* Autophagy is a defense mechanism inhibiting BCG and Mycobacterium tuberculosis survival in infected macrophages. *Cell* **119**, 753-766 (2004).
48. Kimmey, J.M. *et al.* Unique role for ATG5 in neutrophil-mediated immunopathology during M. tuberculosis infection. *Nature* **528**, 565-569 (2015).
49. Divangahi, M. *et al.* Mycobacterium tuberculosis evades macrophage defenses by inhibiting plasma membrane repair. *Nat Immunol* **10**, 899-906 (2009).
50. Mishra, M., Adhyapak, P., Dadhich, R. & Kapoor, S. Dynamic Remodeling of the Host Cell Membrane by Virulent Mycobacterial Sulfoglycolipid-1. *Sci Rep* **9**, 12844 (2019).

51. Brill, S. *et al.* The Ras GTPase-activating-protein-related human protein IQGAP2 harbors a potential actin binding domain and interacts with calmodulin and Rho family GTPases. *Mol Cell Biol* **16**, 4869-4878 (1996).
52. Ho, Y.D., Joyal, J.L., Li, Z. & Sacks, D.B. IQGAP1 integrates Ca2+/calmodulin and Cdc42 signaling. *J Biol Chem* **274**, 464-470 (1999).
53. Atcheson, E. *et al.* IQ-motif selectivity in human IQGAP2 and IQGAP3: binding of calmodulin and myosin essential light chain. *Biosci Rep* **31**, 371-379 (2011).
54. Hart, M.J., Callow, M.G., Souza, B. & Polakis, P. IQGAP1, a calmodulin-binding protein with a rasGAP-related domain, is a potential effector for cdc42Hs. *EMBO J* **15**, 2997-3005 (1996).
55. Joyal, J.L. *et al.* Calmodulin modulates the interaction between IQGAP1 and Cdc42. Identification of IQGAP1 by nanoelectrospray tandem mass spectrometry. *J Biol Chem* **272**, 15419-15425 (1997).
56. Mataraza, J.M. *et al.* IQGAP1 promotes cell motility and invasion. *J Biol Chem* **278**, 41237-41245 (2003).
57. Noritake, J., Watanabe, T., Sato, K., Wang, S. & Kaibuchi, K. IQGAP1: a key regulator of adhesion and migration. *J Cell Sci* **118**, 2085-2092 (2005).
58. Claude-Taupin, A. *et al.* ATG9A Is Overexpressed in Triple Negative Breast Cancer and Its In Vitro Extinction Leads to the Inhibition of Pro-Cancer Phenotypes. *Cells* **7** (2018).
59. Yamano, K., Fogel, A.I., Wang, C., van der Bliek, A.M. & Youle, R.J. Mitochondrial Rab GAPs govern autophagosome biogenesis during mitophagy. *Elife* **3**, e01612 (2014).
60. Mattera, R., Park, S.Y., De Pace, R., Guardia, C.M. & Bonifacino, J.S. AP-4 mediates export of ATG9A from the trans-Golgi network to promote autophagosome formation. *Proc Natl Acad Sci U S A* **114**, E10697-E10706 (2017).
61. Beckwith, K.S. *et al.* Plasma membrane damage causes NLRP3 activation and pyroptosis during Mycobacterium tuberculosis infection. *Nat Commun* **11**, 2270 (2020).
62. Ghosh, S. *et al.* beta-Coronaviruses Use Lysosomes for Egress Instead of the Biosynthetic Secretory Pathway. *Cell* (2020).

Acknowledgments We thank M. Jäätelä and E. Corcelle-Termeau for ATG9A$^{MCF\text{-}7\text{-}KO}$ cells, M. J. Wester for mathematical analysis, M. Campen and T. Young for nanoparticle tracking analysis and UTechS Photonic Bioimaging (supported by ANR-10-INSB-04-01). S.A.T. was supported by the Francis Crick Institute (Cancer Research UK, FC001187), the UK Medical Research Council (FC001187), and the Wellcome Trust (FC001187). F.R. was supported by a ZonMW TOP (91217002) and ALW Open Programme (ALWOP.310) grants. M.C.M. was supported by an ALW Open Program (ALWOP.355) grant. This work

was supported by NIH grants R37AI042999 and R01AI042999, and center grant P20GM121176 to V.D.

Author contributions Conceptualization: A.C.T. and V.D.; Formal Analysis: A.C.T., J.J., Z.B. M.G.T., S.K., G.P.S., R.J., Y.G., L.A., R.P., S.P., F.W., M.S., S.A.T., and V.D.; Investigation and Validation: A.C.T., J.J., Z.B., M.G.T., S.,K., G.P.S., Y.G., L.A., R.P., S.P., F.W., M.S., B.P., M.M., P.V., M.C.M., T.J., and V.D.; Resources: V.D., K.L., Y.U., S.A.T., P.V., T.J., and F.R.; Data Curation: L.A., B.P., A.C.T., and V.D.; Writing – Original Draft: A.C.T. and V.D.; Writing – comments: S.A.T., F.R.; Visualization: A.C.T., S.P., M.C.M., and V.D.; Supervision: V.D., L.J.C., B.P., T.J., F.R.; Project Administration: V.D.; Funding Acquisition: V.D.

Competing interests The authors declare no competing interests.

Additional Information: Supplementary information is available for this paper.

Figure 1. ATG9A protects cells against plasma membrane damage.

a, Plasma membrane (PM) permeabilization/damage quantification by High Content Microscopy (HCM); propidium iodide (PI^+ nuclei) staining. **b,** Immunoblot, $ATG9A^{Huh7\text{-}KO}$ cells. Representative of 3 independent experiments. **c,d,** image examples (white masks, algorithm-defined cell boundaries; yellow masks, computer-identified PI^+ nuclei) (c) and HCM quantification (d) of PM permeabilization (saponin (Sap), digitonin (Dig) or streptolysin O (SLO)) in $ATG9A^{Huh7\text{-}WT}$ and $ATG9A^{Huh7\text{-}KO}$ cells. Data, % of cells positive for PI (mean±SEM; n=5 biologically independent samples, two-way ANOVA Sidak's test). Scale bars, 10 µm. **e,** PMHAL assay schematic, strategy for using HaloTag (HT) probe for quantification of PM permeabilization/damage by HCM. MIL staining is scored, and MPL staining is used as a control for HT probe. **f,** PMHAL images (confocal) of $ATG9A^{Huh7\text{-}WT}$ and $ATG9A^{Huh7\text{-}KO}$ cells, showing MPL and MIL staining with or without PM damage (Dig). Scale bars, 10 µm. **g,** PMHAL assay, HCM quantification (GFP^+MIL^+ puncta intensity) of PM permeabilization in $ATG9A^{Huh7\text{-}WT}$ and $ATG9A^{Huh7\text{-}KO}$ cells subjected to PM damage. Data, mean±SEM; n=5 biologically independent samples, two-way ANOVA Sidak's test. **h,** HCM quantification of PM permeabilization (PI, Dig) of $ATG9A^{Huh7\text{-}WT}$ and $ATG9A^{Huh7\text{-}KO}$ cells washed with 5 mM EGTA and incubated in a Ca^{2+}-free HBSS medium with (+) or without (-) added 3.6 mM Ca^{2+}. Data, % of cells positive for PI (mean±SEM; n=5 biologically independent samples, two-way ANOVA Sidak's test). **i,** Schematic, ATG9A protects cells against PM damage.

Figure 2. ATG9A protects plasma membrane against gasdermin pores.

a, HCM quantification of PM permeabilization (PI staining) and cell viability (Live/Dead^{TM}, Calcein^{+} cells) of ATG9A$^{Huh7\text{-}WT}$ and ATG9A$^{Huh7\text{-}KO}$ cells transfected with FLAG-GSDMD-N-terminal fragment (NT). Data, % of FLAG-positive cells that were PI^{+} or Calcein^{+} (inset). Data, mean±SEM; n=6 biologically independent samples, unpaired t test. **b,** Immunoblotting analysis of ATG9A$^{U2OS\text{-}KO}$ cells and endogenous GSDMD cleavage (GSDMD^{NT}). **c,** Immunoblotting analysis of endogenous GSDMD cleavage (GSDMD^{NT}) in BMM from Atg9a$^{fl/fl}$LysM-Cre^{-} and Atg9a$^{fl/fl}$LysM-Cre^{+} mice. **d,** HCM quantification of PM permeabilization (PI staining) of ATG9A$^{U2OS\text{-}WT}$ and ATG9A$^{U2OS\text{-}KO}$ cells electroporated with LPS to induce endogenous GSDMD cleavage. Data, mean±SEM; n=6 biologically independent samples, one-way ANOVA Tukey's test. **e,** Cell death analysis in supernatants of ATG9A$^{U2OS\text{-}WT}$ and ATG9A$^{U2OS\text{-}KO}$ cells electroporated with LPS. Data, % LDH release (mean±SEM; n=6 biologically independent samples, one-way ANOVA Tukey's test). **f,** HCM quantification of PM permeabilization (PI staining) of Atg9a$^{fl/fl}$-LysMCre- and Cre+ BMMs transfected with LPS to induce endogenous GSDMD cleavage. Data, mean±SEM; n=6 biologically independent samples, one-way ANOVA Tukey's test. **g,** Cell death analysis in supernatants of Atg9a^{KO} (LysMCre+) and Atg9a^{WT} (LysMCre-) BMMs after LPS priming and transfection. Data, % LDH release (mean±SEM; n=6 biologically independent samples, one-way ANOVA Tukey's test). **h,** Schematic, ATG9A protects cells against PM damage.

Figure 3. ATG9A translocates to plasma membrane upon its damage.

a, ATG9A localization in HeLa cells expressing FLAG-ATG9A and MyrPalm-EGFP untreated (Ctrl) or treated with digitonin (Dig). Scale bars, 10 µm. **b,** HCM analysis of FLAG-ATG9A and MyrPalm-EGFP colocalization in HeLa cells, after starvation (EBSS) or PM damage with Dig, SLO, or by glass beads injury (GBI). Data, mean±SEM; n=5 biologically independent samples, one-way ANOVA Dunnett's Dunnett's test. **c,** Super-resolution total internal reflection fluorescence (TIRF) microscopy analysis of FLAG-ATG9A and MyrPalm-EGFP (HeLa). Scale bars, 1 µm. **d,** Stable HEK293T$^{APEX2\text{-}ATG9A}$ cells were exposed (Dig) or not (Ctrl) to PM damage. White arrowheads, PM areas showing deposits of diaminobenzidine (APEX2 activity product) with or without adjacent diaminobenzidine-positive vesicles. Scale bars, 1 µm. **e,** Quantification of % of PM with diaminobenzidine deposits (APEX2-ATG9A) in untreated (Ctrl) and digitonin-(Dig) treated HEK293T$^{APEX2\text{-}ATG9A}$ cells. Data, mean±SEM; n=45 random plasma membrane profiles, unpaired t test. **f,** Images of PM permeabilization (PI; red) in HeLa cells expressing MyrPalm-EGFP (green) and FLAG-ATG9A^{Y8F} (blue). White arrows and arrowheads, FLAG-ATG9A^{Y8F} transfected and untransfected cells, respectively. Scale bars, 10 µm. **g,** HCM quantification of PM permeabilization (PI) in HeLa cells expressing GFP-ATG9A^{WT} or GFP-ATG9A^{Y8F}. Data, mean±SEM; n=5 biologically independent samples, two-way ANOVA Sidak's test).

Figure 4. IQGAP1 partners with ATG9A to protect cells against PM damage.

a, Volcano plot, ATG9A partners and changes in their proximity during PM damage (Dig, HEK293T$^{APEX2\text{-}ATG9A}$). X-axis, log2 fold change (Dig/Ctrl ratio; spectral counts); y-axis, -log10 of p-values, *t*-test (n=3 biological replicates per group). Green and red dots, increase and decrease in proximity to ATG9A after Dig treatment, respectively. Orange dots, values below statistical significance cut-off (p≥0.05). Bubble size represents a normalized value for the total amount of spectral counts for the protein indicated. **b,** CoIP (anti-FLAG) analysis of FLAG-ATG9A and GFP-IQGAP1 (HEK293T) with or without PM damage (Dig, SLO, GBI). One of 3 independent experiments. **c,** GST pulldown analysis using radiolabeled [^{35}S]Myc-IQGAP1 and GST-ATG9A$_{1\text{-}584}$. CBB: Coomassie brilliant blue. Images are representative of 3 biologically independent experiments. Graph, mean±SEM; n=3 independent experiments, unpaired t test. **d,** HCM quantification of PM permeabilization (PI, HeLa IQGAP1 KD). Data, mean±SEM; n=5 biologically independent samples, two-way ANOVA Sidak's test. **e,** Schematic summary of the findings in Figure 4.

Figure 5. ATG9A interacts with ESCRTs.

a, CoIP analysis (anti-FLAG) of GFP-ATG9A and FLAG-TSG101 interactions during PM damage (Dig). One of 3 independent experiments. **b,** BioWeB assay schematic (HEK293T$^{APEX2\text{-}ATG9A}$ tetracycline inducible cells) for capture, elution and detection by immunoblotting of endogenous proteins that are proximal to APEX2-ATG9A in different conditions. **c,** BioWeB analysis of changes in TSG101 proximity to APEX2-ATG9A during PM damage (Dig, SLO, GBI, HEK293T$^{APEX2\text{-}ATG9A}$). **d,** Graph, quantification, ratios of eluted TSG101 band intensities vs. TSG101 in the input relative to panel c (mean±SEM; n=4 biologically independent experiments, unpaired t test). **e,** CoIP analysis (anti-GFP) of FLAG-CHMP4A and GFP-ATG9A interactions during PM damage (Dig, HEK293T). One of 3 independent experiments. **f,** CoIP analysis (anti GFP) of interactions between myc-CHMP4B and GFP-ATG9A during PM damage (Dig, HEK293T). *, Unspecific band. One of 3 independent experiments. **g,h,** Quantification, TIRF microscopy images of mCherry-CHMP4B (red) recruitment to PM (MyrPalm-EGFP, green) during PM damage (Dig), in ATG9A$^{Huh7\text{-}WT}$ cells pretreated with NEM or NEM+DTT. **g,** CHMP4B total fluorescence intensity and **h,** CHMP4B puncta number in TIRF field. Data, mean±SEM; n=5 independent images, unpaired t test. **i-k** TIRF microscopy images **(i)** and quantification **(j,k)** of mCherry-CHMP4B (red) recruitment to PM (MyrPalm-EGFP, green) following damage (Dig) in ATG9A$^{Huh7\text{-}WT}$ and ATG9A$^{Huh7\text{-}KO}$ cells. Scale bars, 5 µm. **j,** Data, CHMP4B total fluorescence intensity and **k,** CHMP4B puncta number in TIRF field, mean±SEM; n=5 biologically independent samples, unpaired t test. **l,** HCM quantification of mCherry-CHMP4B overlap with PM (MyrPalm-EGFP) in cells washed with 5 mM EGTA and incubated in a Ca^{2+}-free HBSS medium with (+) or without (-) added 3.6 mM Ca^{2+} during PM damage (Dig). Data, overlap area between CHMP4B and MyrPalm, mean±SEM; n=4 biologically independent samples, one-way ANOVA Tukey's test.

Figure 6. ESCRTs and ATG9A cooperate in protection against plasma membrane damage.

a, Confirmation by immunoblotting of ALIX and TSG101 KDs as well as CRISPR-Cas9 KO of ALIX in HeLa cells. One of 3 independent experiments. **b,** Example of HCM images of PM permeabilization (PI, Dig) in HeLa cells after KD of ALIX, TSG101, ALIX+TSG101 or CRISPR-Cas9 KO of ALIX; white masks, algorithm-defined cell boundaries; red masks, computer-identified PI^+ nuclei. Scale bars, 10 µm. **c,** HCM quantification of PM permeabilization (PI, Dig, HeLa) after KD of ALIX, TSG101, ALIX+TSG101 or in ALIX CRISPR knockout ($ALIX^{KO}$) and $ALIX^{WT}$ HeLa. Data, mean±SEM; n=6 biologically independent samples, one-way ANOVA Tukey's test. **d,** Confirmation by immunoblotting of CHMP2A KD in $ATG9A^{Huh7\text{-}WT}$ and $ATG9A^{Huh7\text{-}KO}$ cells (one of 3 independent experiments). **e,** Example of HCM images of PM permeabilization (PI, Dig) in $ATG9A^{Huh7\text{-}WT}$ and $ATG9A^{Huh7\text{-}KO}$ cells after KD of CHMP2A. White masks, algorithm-defined cell boundaries; red masks, computer-identified PI-positive nuclei. Scale bars, 10 µm. **f,** HCM quantification of PM permeabilization (PI, Dig) in $ATG9A^{Huh7\text{-}WT}$ and $ATG9A^{Huh7\text{-}KO}$ cells after KD of CHMP2A. Data, mean±SEM; n=6 biologically independent samples, unpaired t test. **g,** HCM quantification of PM permeabilization (PI, FLAG-GSDMD-Full length (FL) or –NT fragment transfection) in $ATG9A^{Huh7\text{-}WT}$ and $ATG9A^{Huh7\text{-}KO}$ cells after CHMP2A KD. Data, % of $FLAG^+$ cells that were PI^+ (mean±SEM; n=6 biologically independent samples, unpaired t test). **h,i,** GST-pulldown analysis of in vitro translated and radiolabeled [35S]Myc-IQGAP1 with GST, GST-CHMP2A and GST-CHMP4B fusions. CBB: Coomassie brilliant blue. **i,** Graph, quantification of the binding percentage of IQGAP1 relative to GST constructs. Data, mean±SEM; n=3 biologically independent experiments, unpaired t test. **j,** Schematic summary of findings in Figures 5 and 6.

Figure 7. ATG9A protects against plasma membrane damage in diverse biological contexts.

a, Nanoparticle tracking analysis. Concentration (y-axis) and size distribution (x-axis) of enriched extracellular vesicles in supernatants after PM (Dig) from ATG9A$^{Huh7\text{-}WT}$ (Ctrl: blue; Dig: green) and ATG9A$^{Huh7\text{-}KO}$ (Ctrl: pink; Dig: red) cells. One of 3 independent experiments. **b,** % of particles in 10-88 nm (G1 in a) and 89 -350 nm (G2 in a) after PM damage (Dig). Data, nanoparticle sizing (>800 frames/sample), n=3 biologically independent experiments; mean±SEM; two-way ANOVA Sidak's test. **c,** HCM quantification of PM permeabilization (PI) in ATG9A$^{Huh7\text{-}WT}$ and ATG9A$^{Huh7\text{-}KO}$ cells expressing Hras$_{25}$ PM-targeted MLKL-Venus (PM) or non-targeted MLKL-Venus (NT). Data, % of Venus^{+} cells positive for PI (means ± SEM, n=5 biologically independent samples, two-way ANOVA Sidak's test). **d,** HCM quantification of PM permeabilization (PI), in ATG9A$^{Huh7\text{-}WT}$ and ATG9A$^{Huh7\text{-}KO}$ cells expressing SARS-CoV-2 FLAG-ORF3a. Data, % of cells positive for PI (mean±SEM, n=6 biologically independent samples, two-way ANOVA Tukey's test). **e,** HCM complementation analysis of PM sensitivity to permeabilization by SARS-CoV-2 ORF3a in ATG9A$^{Huh7\text{-}KO}$ cells co-transfected with SARS-CoV-2-GFP-ORF3a and ATG9A-FLAG (WT or M33 scramblase mutant). PI^{+} cells quantified after gating on GFP^{+} cells (HCM, mean± SEM, n=6 biologically independent samples, one-way ANOVA Tukey's test). **f,** HCM quantification of PM permeabilization (PI), in ATG9A$^{Huh7\text{-}WT}$ and ATG9A$^{Huh7\text{-}KO}$ cells exposed to virulent *Mycobacterium tuberculosis* Erdman. Multiplicity of infection (MOI): 0 (Ctrl), 5 or 10; 1h. Data, % of cells positive for PI (mean±SEM, n=6 biologically independent samples, two-way ANOVA Sidak's test). **g,** Overall schematic summary. Upon PM damage, ATG9A (recruited by Ca^{2+} influx and IQGAP1) organizes ESCRT machinery at the site of injury where ESCRT-III effectors (CHMP4A/B and CHMP2A) remodel membranes to bud EVs carrying away the PM pore/damaged area.

Fig1

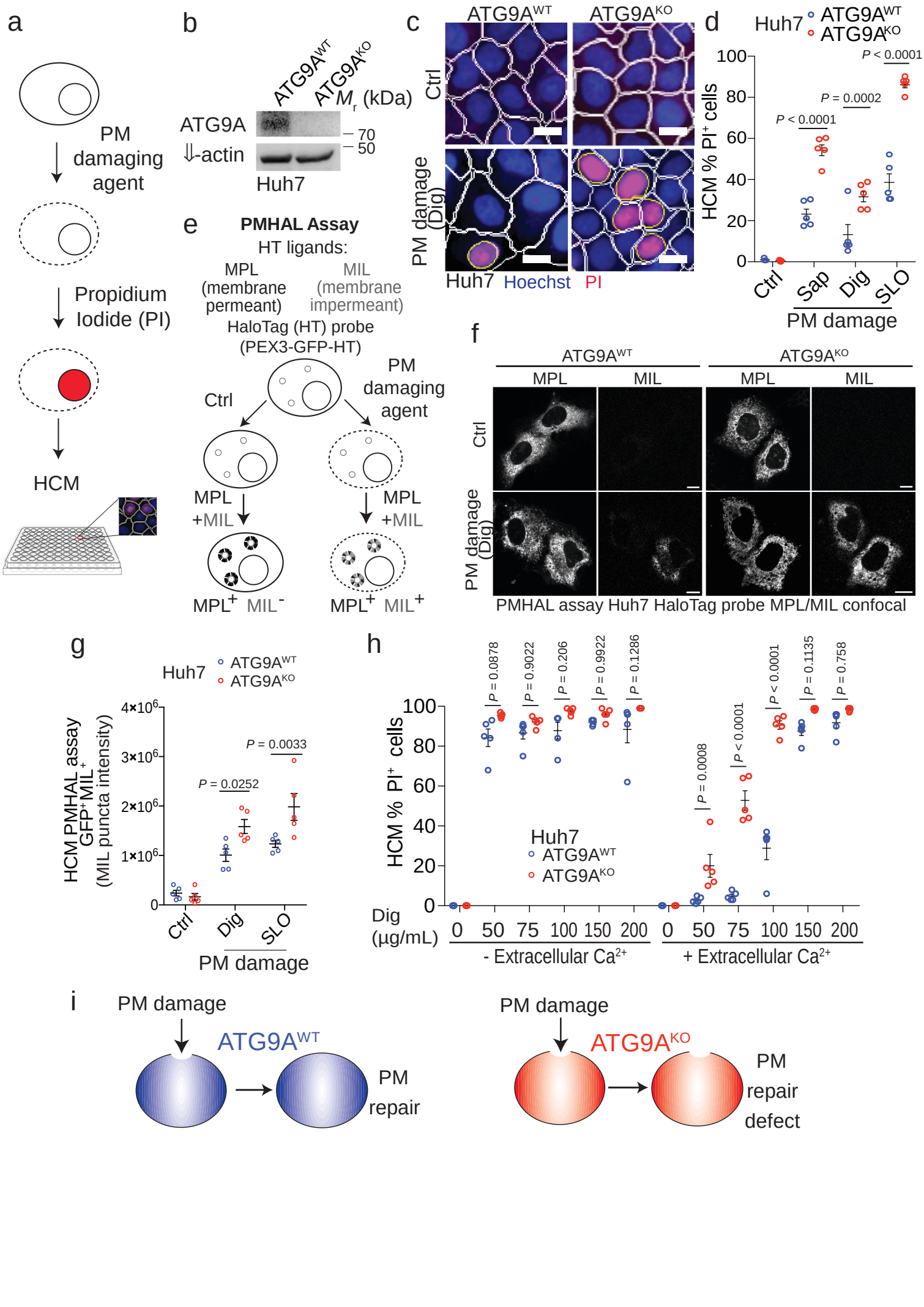
a
PM damaging agent
Propidium Iodide (PI)
HCM
b
ATG9A^WT
ATG9A^KO
M_r (kDa)
ATG9A
⇓-actin
70
50
Huh7
c
ATG9A^WT
ATG9A^KO
Ctrl
PM damage (Dig)
Huh7 Hoechst PI
d
Huh7
ATG9A^WT
ATG9A^KO
HCM % PI+ cells
P < 0.0001
P = 0.0002
P < 0.0001
Ctrl
Sap
Dig
SLO
PM damage
e
PMHAL Assay
HT ligands:
MPL (membrane permeant)
MIL (membrane impermeant)
HaloTag (HT) probe (PEX3-GFP-HT)
Ctrl
PM damaging agent
MPL +MIL
MPL+ MIL-
MPL+ MIL+
f
ATG9A^WT
ATG9A^KO
MPL
MIL
Ctrl
PM damage (Dig)
PMHAL assay Huh7 HaloTag probe MPL/MIL confocal
g
Huh7
ATG9A^WT
ATG9A^KO
HCM PMHAL assay GFP+MIL+ (MIL puncta intensity)
P = 0.0252
P = 0.0033
Ctrl
Dig
SLO
PM damage
h
HCM % PI+ cells
P = 0.0878
P = 0.9022
P = 0.206
P = 0.9922
P = 0.1286
P = 0.0008
P < 0.0001
P < 0.0001
P = 0.1135
P = 0.758
Huh7
ATG9A^WT
ATG9A^KO
Dig (µg/mL)
0 50 75 100 150 200
- Extracellular Ca2+
+ Extracellular Ca2+
i
PM damage
ATG9A^WT
PM repair
PM damage
ATG9A^KO
PM repair defect

Fig2

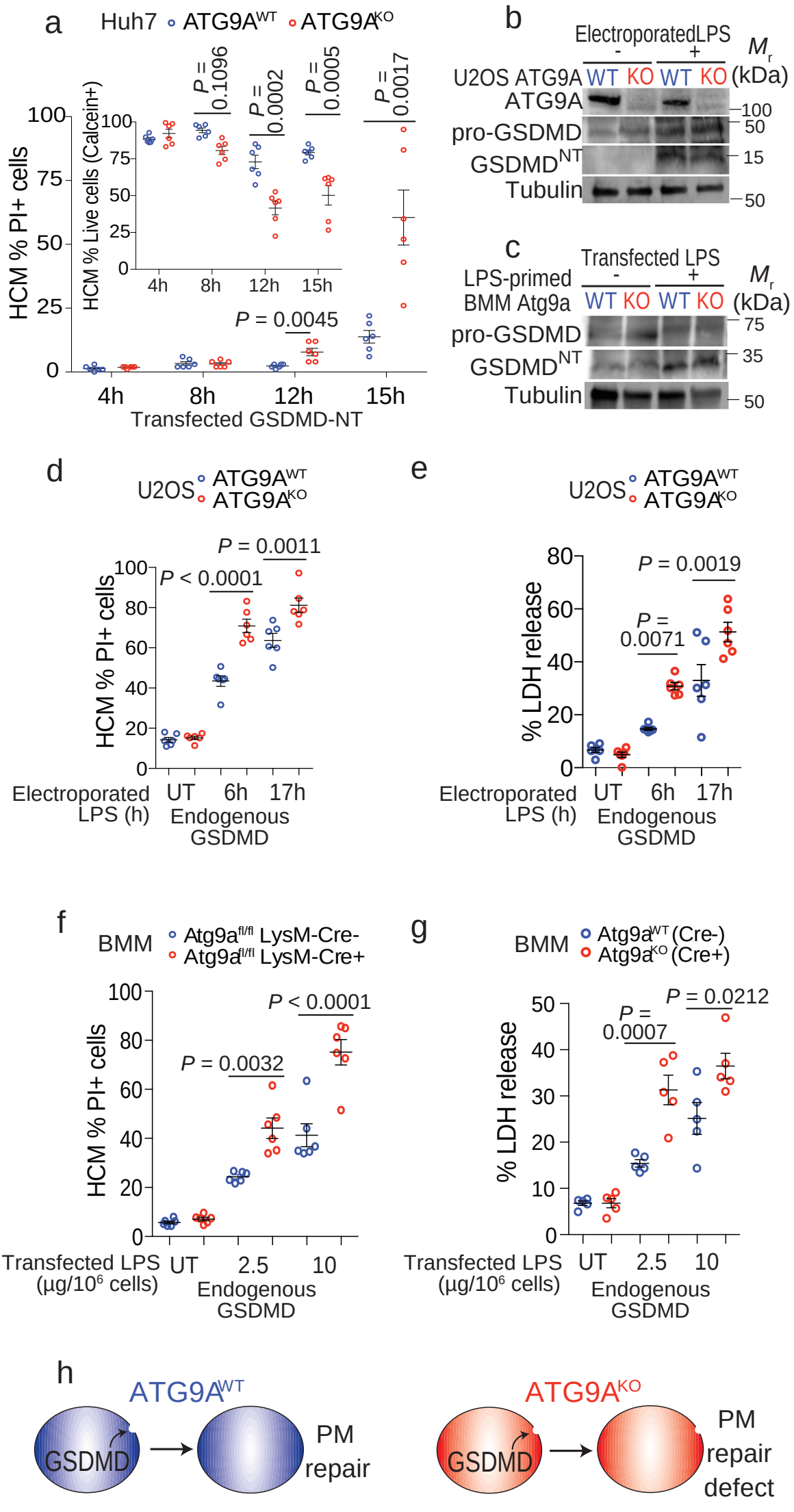
a
Huh7 ATG9A^WT ATG9A^KO
HCM % PI+ cells
HCM % Live cells (Calcein+)
P = 0.1096
P = 0.0002
P = 0.0005
P = 0.0017
P = 0.0045
4h
8h
12h
15h
Transfected GSDMD-NT
b
ElectroporatedLPS
U2OS ATG9A WT KO WT KO (kDa)
ATG9A
pro-GSDMD
GSDMD^NT
Tubulin
c
Transfected LPS
LPS-primed BMM Atg9a WT KO WT KO (kDa)
pro-GSDMD
GSDMD^NT
Tubulin
d
U2OS ATG9A^WT ATG9A^KO
P = 0.0011
P < 0.0001
HCM % PI+ cells
Electroporated LPS (h)
UT
6h
17h
Endogenous GSDMD
e
U2OS ATG9A^WT ATG9A^KO
P = 0.0019
P = 0.0071
% LDH release
Electroporated LPS (h)
UT
6h
17h
Endogenous GSDMD
f
BMM Atg9a^fl/fl LysM-Cre- Atg9a^fl/fl LysM-Cre+
P < 0.0001
P = 0.0032
HCM % PI+ cells
Transfected LPS (µg/10^6 cells)
UT
2.5
10
Endogenous GSDMD
g
BMM Atg9a^WT (Cre-) Atg9a^KO (Cre+)
P = 0.0212
P = 0.0007
% LDH release
Transfected LPS (µg/10^6 cells)
UT
2.5
10
Endogenous GSDMD
h
ATG9A^WT
GSDMD
PM repair
ATG9A^KO
GSDMD
PM repair defect

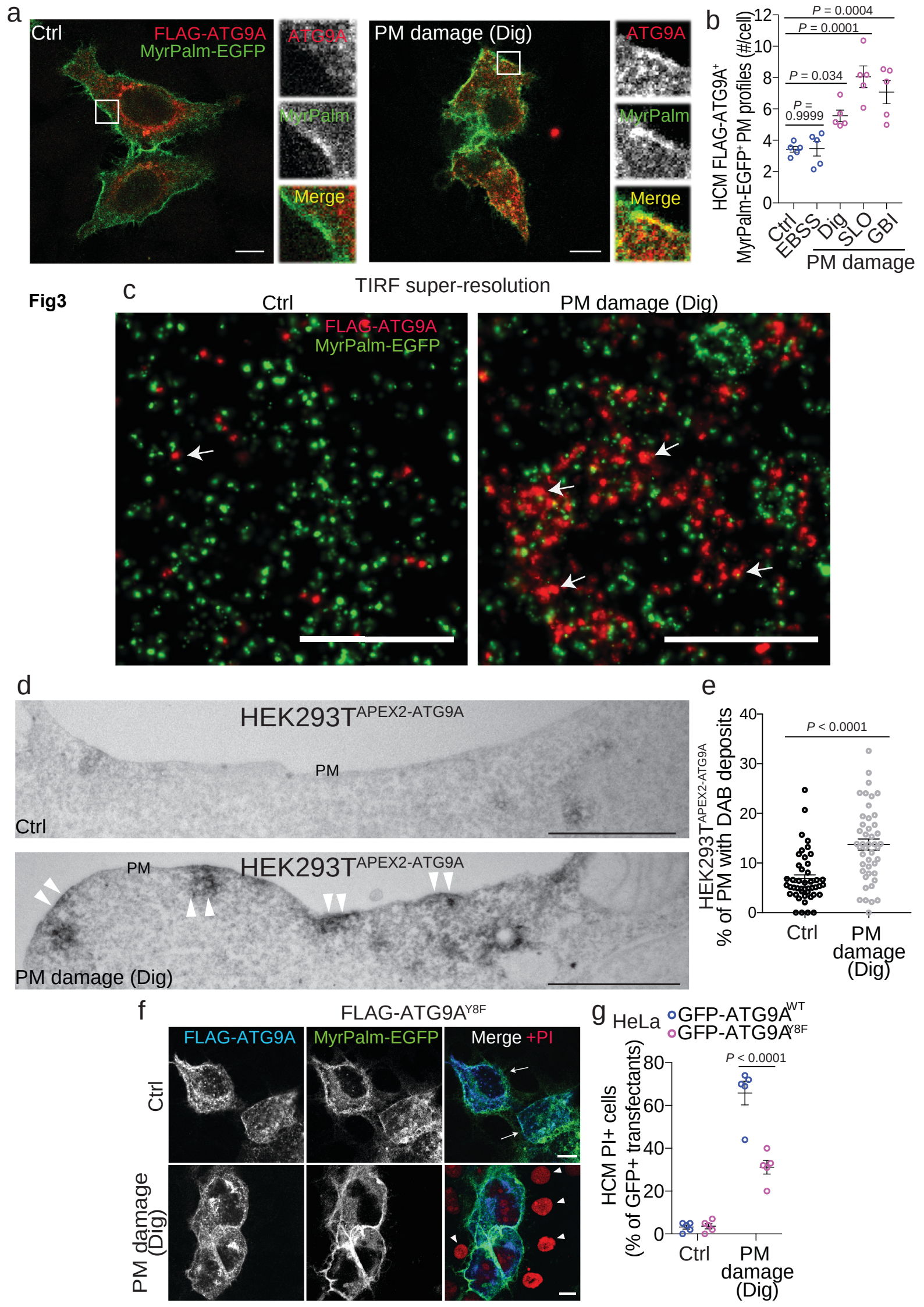
a
Ctrl
FLAG-ATG9A
MyrPalm-EGFP
ATG9A
MyrPalm
Merge
PM damage (Dig)
ATG9A
MyrPalm
Merge
b
P = 0.0004
P = 0.0001
P = 0.034
P = 0.9999
HCM FLAG-ATG9A+ MyrPalm-EGFP+ PM profiles (#/cell)
0
2
4
6
8
10
12
Ctrl
EBSS
Dig
SLO
GBI
PM damage
Fig3
c
TIRF super-resolution
Ctrl
PM damage (Dig)
FLAG-ATG9A
MyrPalm-EGFP
d
HEK293TAPEX2-ATG9A
PM
Ctrl
PM
HEK293TAPEX2-ATG9A
PM damage (Dig)
e
P < 0.0001
HEK293TAPEX2-ATG9A % of PM with DAB deposits
0
10
20
30
40
Ctrl
PM damage (Dig)
f
FLAG-ATG9AY8F
FLAG-ATG9A
MyrPalm-EGFP
Merge +PI
Ctrl
PM damage (Dig)
g
HeLa
GFP-ATG9AWT
GFP-ATG9AY8F
P < 0.0001
HCM PI+ cells (% of GFP+ transfectants)
0
20
40
60
80
Ctrl
PM damage (Dig)

Fig4

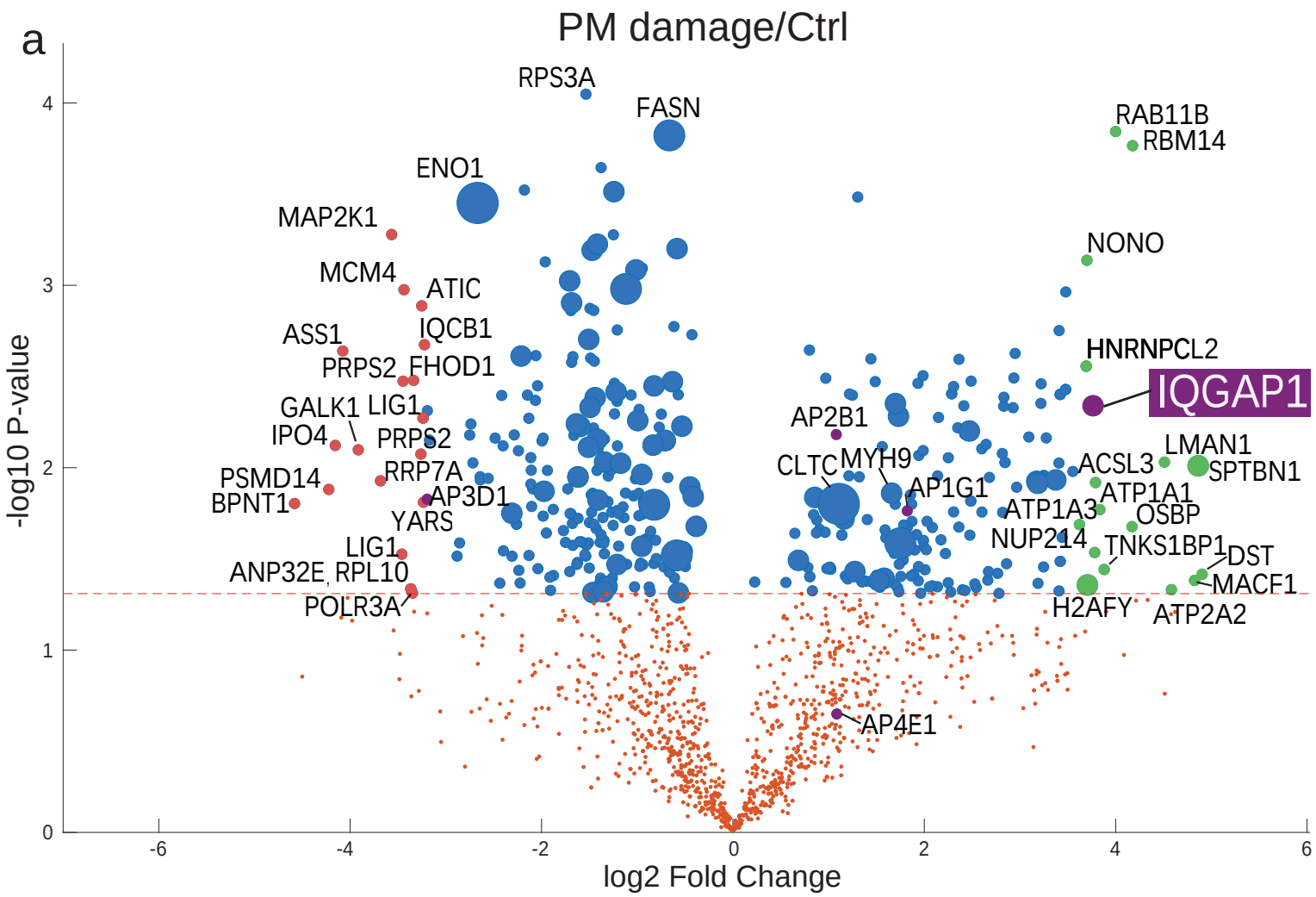
a
PM damage/Ctrl
-log10 P-value
log2 Fold Change
RPS3A
FASN
ENO1
MAP2K1
MCM4
ATIC
IQCB1
ASS1
PRPS2
FHOD1
GALK1
LIG1
IPO4
PRPS2
RRP7A
PSMD14
BPNT1
AP3D1
YARS
LIG1
ANP32E
RPL10
POLR3A
RAB11B
RBM14
NONO
HNRNPCL2
IQGAP1
AP2B1
CLTC
MYH9
AP1G1
ACSL3
LMAN1
SPTBN1
ATP1A1
ATP1A3
OSBP
NUP214
TNKS1BP1
DST
MACF1
H2AFY
ATP2A2
AP4E1

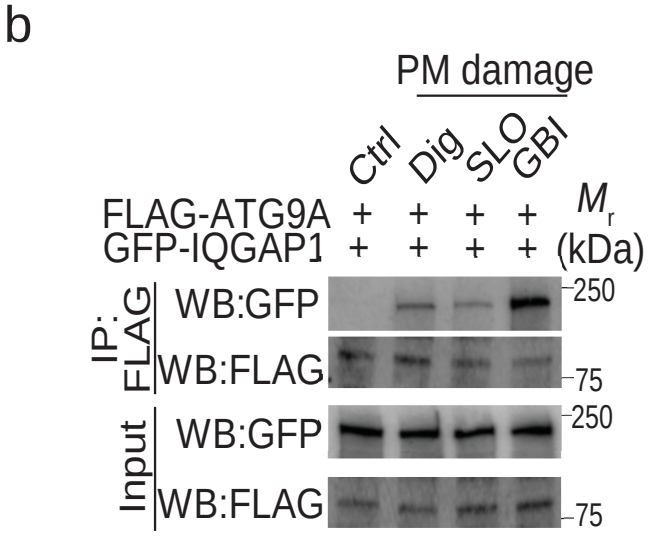
b
PM damage
Ctrl
Dig
SLO
GBI
FLAG-ATG9A + + + +
GFP-IQGAP1 + + + +
Mr (kDa)
IP: FLAG
WB:GFP
WB:FLAG
Input
WB:GFP
WB:FLAG
250
75
250
75

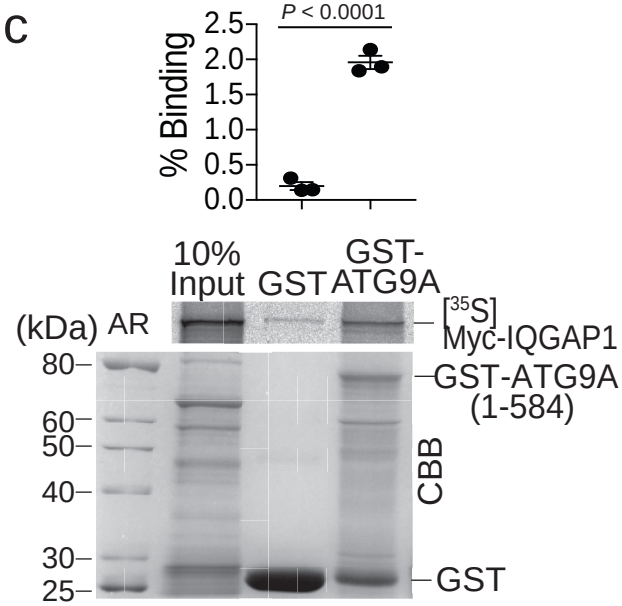
c
P < 0.0001
% Binding
10% Input
GST
GST-ATG9A
(kDa)
AR
[35S] Myc-IQGAP1
GST-ATG9A (1-584)
CBB
GST
80
60
50
40
30
25

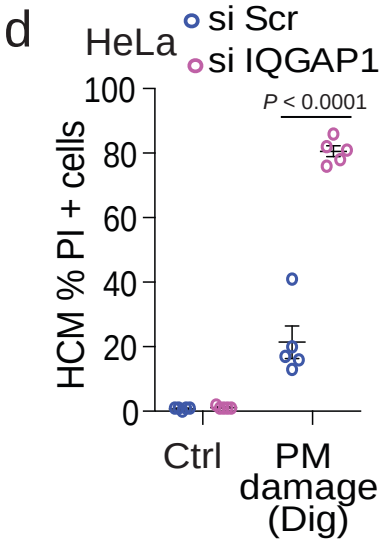
d
HeLa
si Scr
si IQGAP1
P < 0.0001
HCM % PI + cells
Ctrl
PM damage (Dig)

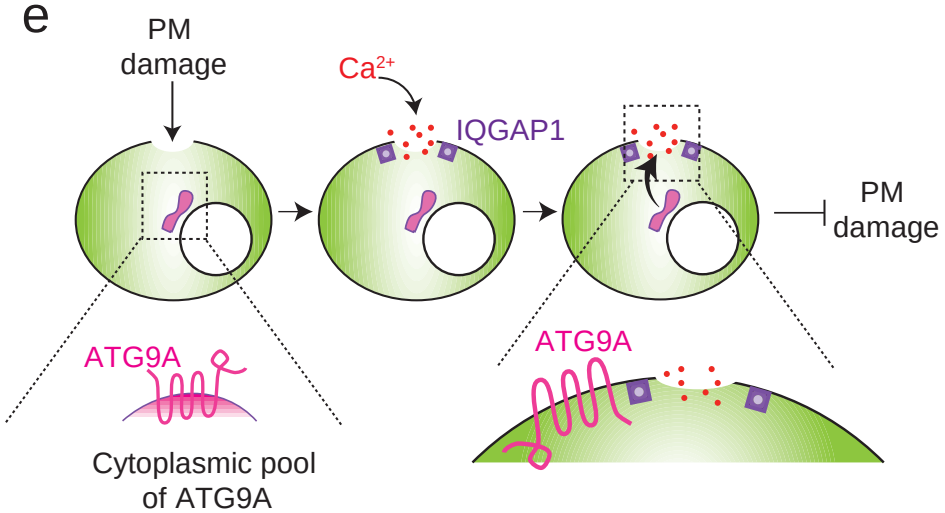
e
PM damage
Ca2+
IQGAP1
PM damage
ATG9A
Cytoplasmic pool of ATG9A
ATG9A

Fig5

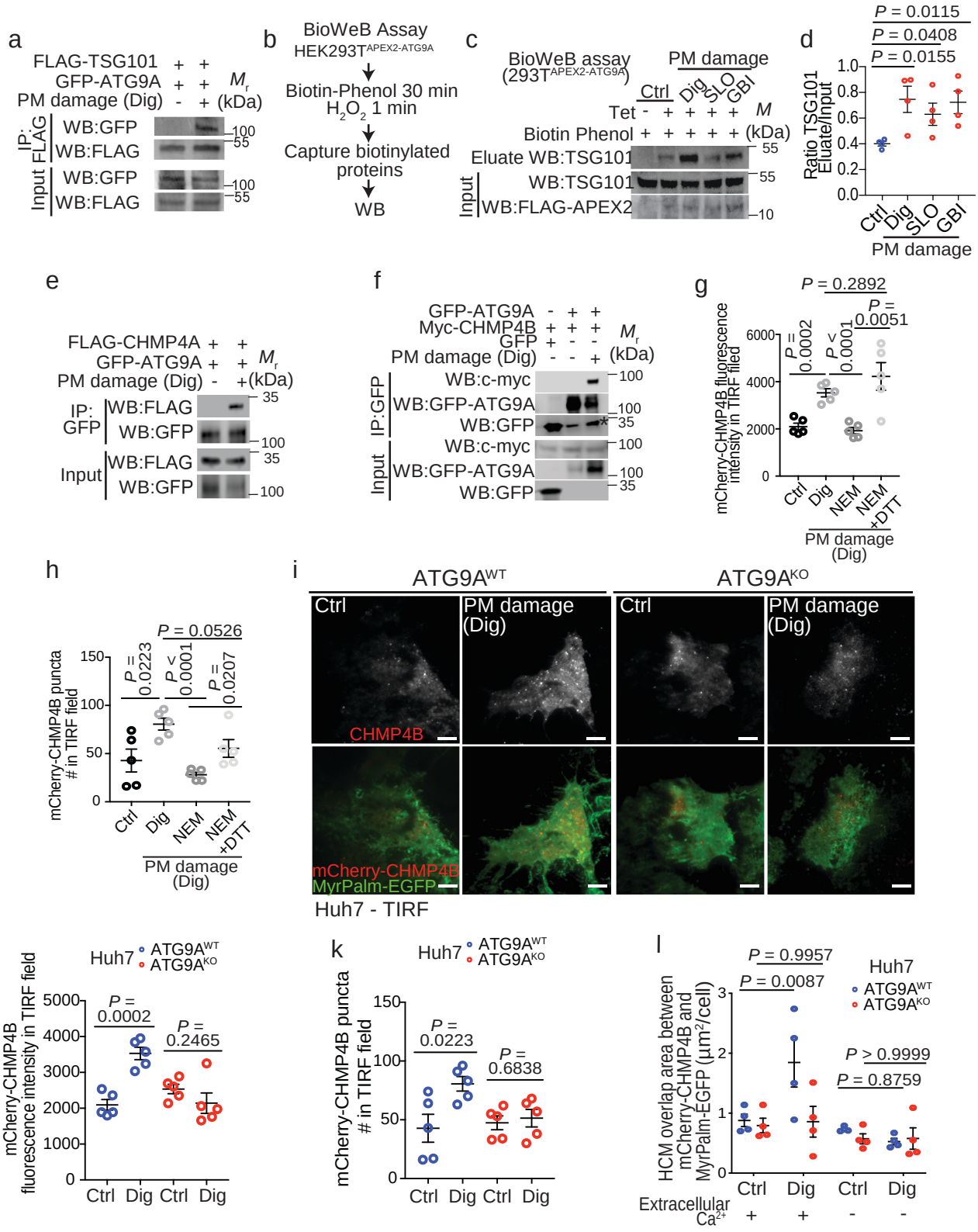
a
FLAG-TSG101 + +
GFP-ATG9A + +
PM damage (Dig) - +
Mr (kDa)
IP: FLAG
WB:GFP
WB:FLAG
Input
WB:GFP
WB:FLAG
100
55
100
55
b
BioWeB Assay
HEK293T APEX2-ATG9A
Biotin-Phenol 30 min
H2O2 1 min
Capture biotinylated proteins
WB
c
BioWeB assay (293T APEX2-ATG9A)
PM damage
Ctrl
Dig
SLO
GBI
Tet - + + + +
M (kDa)
Biotin Phenol + + + + +
Eluate WB:TSG101
55
Input
WB:TSG101
55
WB:FLAG-APEX2
10
d
P = 0.0115
P = 0.0408
P = 0.0155
Ratio TSG101 Eluate/Input
1.0
0.8
0.6
0.4
0.2
0.0
Ctrl
Dig
SLO
GBI
PM damage
e
FLAG-CHMP4A + +
GFP-ATG9A + +
PM damage (Dig) - +
Mr (kDa)
IP: GFP
WB:FLAG
WB:GFP
35
100
Input
WB:FLAG
WB:GFP
35
100
f
GFP-ATG9A - + +
Myc-CHMP4B + + +
GFP + - -
PM damage (Dig) - - +
Mr (kDa)
IP:GFP
WB:c-myc
WB:GFP-ATG9A
WB:GFP
100
100
35
*
Input
WB:c-myc
WB:GFP-ATG9A
WB:GFP
100
100
35
g
P = 0.2892
P = 0.0051
P = 0.0002
P < 0.0001
mCherry-CHMP4B fluorescence intensity in TIRF filed
6000
4000
2000
0
Ctrl
Dig
NEM
NEM +DTT
PM damage (Dig)
h
P = 0.0526
P = 0.0223
P < 0.0001
P = 0.0207
mCherry-CHMP4B puncta # in TIRF field
150
100
50
0
Ctrl
Dig
NEM
NEM +DTT
PM damage (Dig)
i
ATG9AWT
ATG9AKO
Ctrl
PM damage (Dig)
Ctrl
PM damage (Dig)
CHMP4B
mCherry-CHMP4B
MyrPalm-EGFP
Huh7 - TIRF
j
Huh7 ATG9AWT ATG9AKO
mCherry-CHMP4B fluorescence intensity in TIRF field
5000
4000
3000
2000
1000
0
P = 0.0002
P = 0.2465
Ctrl Dig Ctrl Dig
k
Huh7 ATG9AWT ATG9AKO
mCherry-CHMP4B puncta # in TIRF field
150
100
50
0
P = 0.0223
P = 0.6838
Ctrl Dig Ctrl Dig
l
P = 0.9957
P = 0.0087
Huh7
ATG9AWT
ATG9AKO
P > 0.9999
P = 0.8759
HCM overlap area between mCherry-CHMP4B and MyrPalm-EGFP (μm²/cell)
3
2
1
0
Ctrl Dig Ctrl Dig
Extracellular Ca2+ + + - -

Fig6

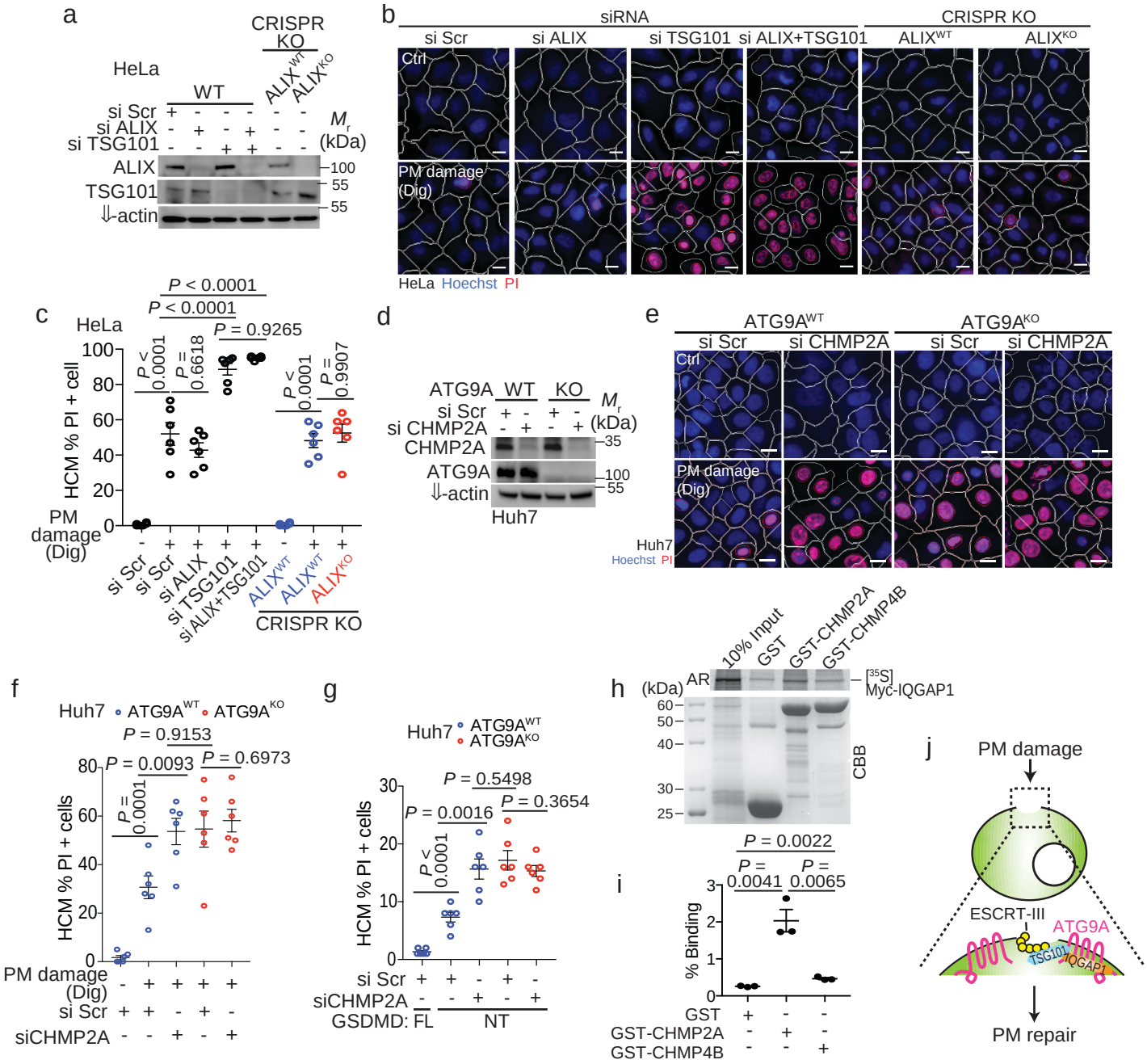
a
HeLa
CRISPR KO
WT
ALIX^WT
ALIX^KO
si Scr
si ALIX
si TSG101
M_r (kDa)
ALIX
TSG101
⇓-actin
100
55
55
b
siRNA
CRISPR KO
si Scr
si ALIX
si TSG101
si ALIX+TSG101
ALIX^WT
ALIX^KO
Ctrl
PM damage (Dig)
HeLa Hoechst PI
c
HeLa
P < 0.0001
P < 0.0001
P = 0.9265
P < 0.0001
P = 0.6618
P < 0.0001
P = 0.9907
HCM % PI + cell
PM damage (Dig)
si Scr
si Scr
si ALIX
si TSG101
si ALIX+TSG101
ALIX^WT
ALIX^WT
ALIX^KO
CRISPR KO
d
ATG9A WT KO
si Scr
si CHMP2A
CHMP2A
ATG9A
⇓-actin
M_r (kDa)
35
100
55
Huh7
e
ATG9A^WT
ATG9A^KO
si Scr
si CHMP2A
si Scr
si CHMP2A
Ctrl
PM damage (Dig)
Huh7
Hoechst PI
f
Huh7 ATG9A^WT ATG9A^KO
P = 0.9153
P = 0.0093
P = 0.6973
P = 0.0001
HCM % PI + cells
PM damage (Dig)
si Scr
siCHMP2A
g
Huh7 ATG9A^WT ATG9A^KO
P = 0.5498
P = 0.0016
P = 0.3654
P < 0.0001
HCM % PI + cells
si Scr
siCHMP2A
GSDMD: FL
NT
h
10% Input
GST
GST-CHMP2A
GST-CHMP4B
(kDa)
AR
[35S] Myc-IQGAP1
60
50
40
30
25
CBB
i
P = 0.0022
P = 0.0041
P = 0.0065
% Binding
GST
GST-CHMP2A
GST-CHMP4B
j
PM damage
ESCRT-III
ATG9A
TSG101
IQGAP1
PM repair

Fig7

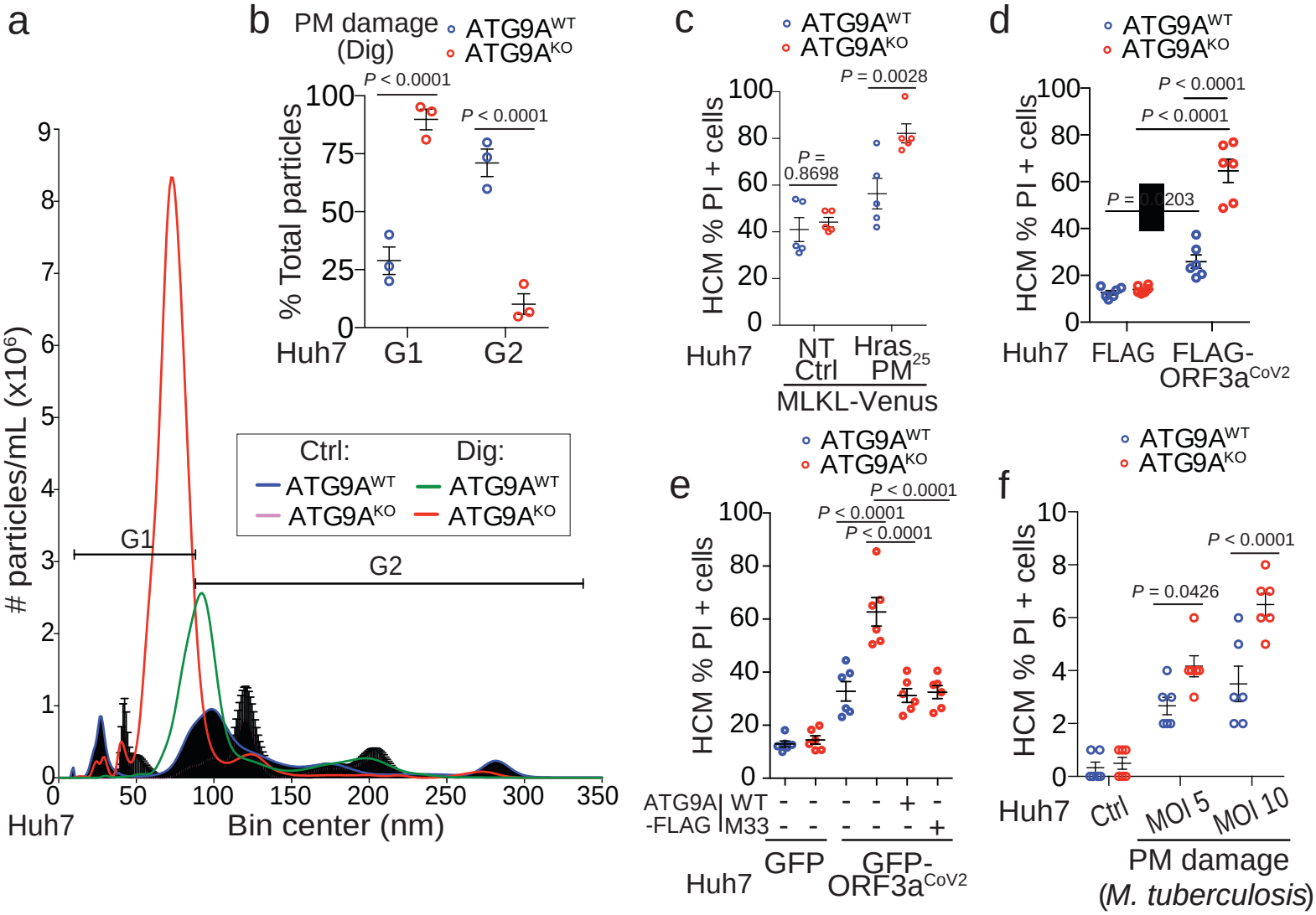
a
b
PM damage (Dig)
ATG9A^WT
ATG9A^KO
P < 0.0001
P < 0.0001
% Total particles
Huh7
G1
G2
particles/mL (x10^6)
Ctrl:
Dig:
ATG9A^WT
ATG9A^KO
ATG9A^WT
ATG9A^KO
G1
G2
Bin center (nm)
c
ATG9A^WT
ATG9A^KO
P = 0.0028
P = 0.8698
HCM % PI + cells
Huh7
NT Ctrl
Hras PM25
MLKL-Venus
d
ATG9A^WT
ATG9A^KO
P < 0.0001
P < 0.0001
P = 0.0203
HCM % PI + cells
Huh7
FLAG
FLAG-ORF3a^CoV2
e
ATG9A^WT
ATG9A^KO
P < 0.0001
P < 0.0001
P < 0.0001
HCM % PI + cells
ATG9A -FLAG
WT
M33
Huh7
GFP
GFP-ORF3a^CoV2
f
ATG9A^WT
ATG9A^KO
P < 0.0001
P = 0.0426
HCM % PI + cells
Huh7
Ctrl
MOI 5
MOI 10
PM damage (M. tuberculosis)

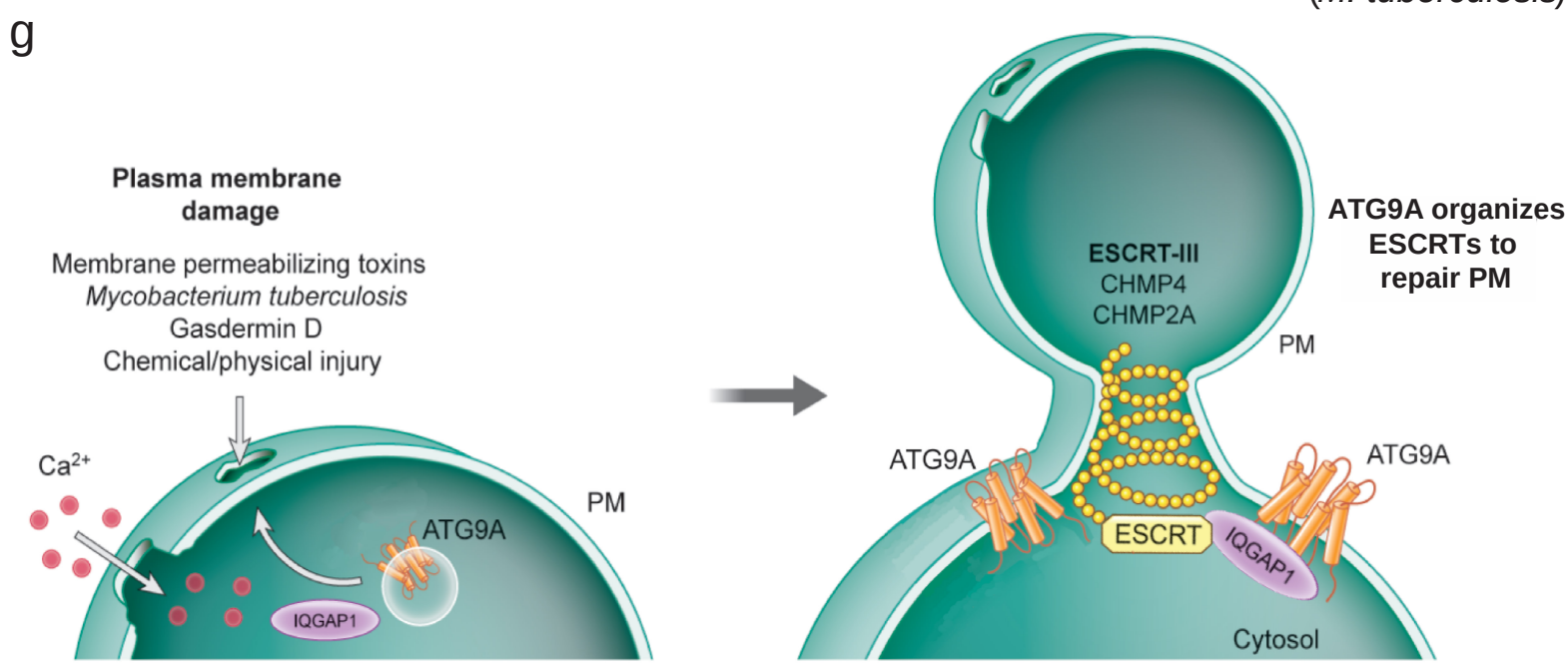
g
Plasma membrane damage
Membrane permeabilizing toxins
Mycobacterium tuberculosis
Gasdermin D
Chemical/physical injury
Ca2+
PM
ATG9A
IQGAP1
ESCRT-III
CHMP4
CHMP2A
PM
ATG9A
ATG9A
ESCRT
IQGAP1
Cytosol
ATG9A organizes ESCRTs to repair PM

Methods

Antibodies and reagents

Antibodies from Abcam were GFP (ab290) (1:1000 for WB), GFP (ab38689) (1:100 for immunoprecipitation (IP)), GM130 (ab1299) (1:1000 for WB), GSDMD (ab209845, for BMMs) (1:1000 for WB), PDCD6/ALG-2 (ab133326) (1:1000 for WB), RAB7 (ab137029) (1:1000 for WB) and TSG101(ab83) (1:1000 for WB). ALIX antibody was from BioLegend (#634502) (1:1000 for WB; 1:500 for IF) and CD63 antibody from BD (#556019) (1:500 for WB). Antibodies from Cell Signaling Technology were ATG9A (#13509) (1:1000 for WB), IQGAP1 (#20648) (1:1000 for WB; 1:500 for IF). Other antibodies used in this study were from the following sources: FLAG M2 (F1804) (1:1000 for WB, 1:100 for IP), GSDMD (G7422, for U2OS) (1:1000 for WB), LC3B (L7543) (1:2000 for WB), PI4KB (06-578) (1:1000 for WB) from Sigma Aldrich; beta-actin (C4) (1:1000 for WB), c-myc (sc-40) (1:500 for WB), HA-probe (12CA5) (1:1000 for WB) from Santa Cruz Biotechnology; ATG2A (23226-1-AP) (1:1000 for WB), ATG2B (25155-1-AP) (1:1000 for WB), CHMP2A (10477-1-AP) (1:500 for WB) from Proteintech. HRP-labeled anti-rabbit (sc-2004) (1:2000 for WB) and anti-mouse (sc-2005) (1:2000 for WB) secondary antibodies, anti-rabbit Alexa Fluor-488 (A-11034); -568 (A-11036); -647 (A-21245) and anti-mouse Alexa Fluor -488 (A-11029); -568 (A-11004); -647 (A-21235) (1:500 for IF), from ThermoFisher Scientific. Membrane-impermeable HaloTag Ligand (MIL) (Promega, Alexa Fluor 660-conjugated, G8471) (1:1000 for IF), Membrane-permeable HaloTag Ligand (MPL) (Promega, tetramethylrhodamine-conjugated, G8251) (1:1000 for IF). Saponin (S4521), digitonin (D5628), streptolysin O (SLO; SAE0089) and acid-washed glass beads (diam. ~0.5 mm, G8772) were purchased from Sigma Aldrich. Propidium iodide solution (10008351) was purchased from Cayman Chemical. Dextran 10k fluorescein (D1820), DQ Red BSA (D12051) and CellMask Deep Red plasma membrane stain (C10046) (1:1000 for IF) were purchased from ThermoFisher Scientifc. DMEM, RPMI, OptiMEM and EBSS medias from Life Technologies.

Cells and cell lines

HEK293T and HeLa cells were from ATCC. The Huh7 cell line was purchased from Rocky Mountain Laboratory. Bone marrow-derived macrophages (BMMs) were isolated from femurs of $Atg9a^{fl/fl}$ $LysM\text{-}Cre^{+}$ mice and its Cre-negative littermates[63] were cultured in DMEM supplemented with mouse macrophage colony stimulating factor (mM-CSF, #5228, CST). Mice were cared following protocols approved by Institutional Animal Care and Use Committee. HEK293T Flp-In-FLAG-APEX2-$ATG9A^{TetON}$ ($HEK293T^{APEX2\text{-}ATG9A}$) and Hela Flp-In-mCherry-CHMP4A were generated using a modified gateway construct from Terje Johansen. MCF-7 ATG9A CRISPR KO ($ATG9A^{MCF\text{-}7\text{-}KO}$) cells and their parental MCF-7 WT ($ATG9A^{MCF\text{-}7\text{-}WT}$) cells were a kind gift from Marja Jäättelä (University of Copenhagen). MCF-7 cells were from Marja Jäättelä. Huh7 ATG9A CRISPR KO ($ATG9A^{Huh7\text{-}KO}$) cells and their parental Huh7 ATG9A WT ($ATG9A^{Huh7\text{-}WT}$) were generated by transduction of two ATG9A CRISPR-Cas9 gRNAs. An identical approach was used to generate U2OS cells lacking ATG9A ($ATG9A^{U2OS\text{-}KO}$), ATG2A ($ATG2A^{U2OS\text{-}KO}$) or ATG2B ($ATG2B^{U2OS\text{-}KO}$). These cells were a kind gift from Fulvio Reggiori. U2OS cells were a kind gift from Prof. Ger Strous (University Medical Center Utrecht, The Netherlands). HeLa

ALIX CRISPR KO ($ALIX^{HeLa\text{-}KO}$) and their parental Hela ALIX WT ($ALIX^{HeLa\text{-}WT}$) were generated by transduction of one CRISPR-Cas9 gRNA.

Plasmids, siRNAs, and transfection

Plasmids used in this study for immunoprecipitation or immunofluorescence assays, such as those expressing ATG9A, ALIX (including their mutants' deletions) and CHMP4A were cloned into pDONR221 (Gateway Technology cloning vector, Thermo Scientific) using a BP cloning reaction. Expression vectors were then made by an LR cloning reaction (Gateway, ThermoFisher) in appropriate destination (pDEST) vectors.

ATG9A mutants were generated utilizing the QuikChange site-directed mutagenesis kit (Agilent) and confirmed by sequencing (Genewiz). siRNAs were from GE Dharmacon (siGENOME SMART pool). Plasmid transfections were performed using the calcium phosphate transfection method in HEK293T cells or using lipofectamine 2000 in the other cell lines (ThermoFisher Scientific). siRNAs were delivered into cells using Lipofectamine RNAiMAX (ThermoFisher Scientific).

Generating cell lines by CRISPR/Cas9

ATG9A (($ATG9A^{Huh7\text{-}KO}$ and $ATG9A^{U2OS\text{-}KO}$), ATG2A ($ATG2A^{U2OS\text{-}KO}$), ATG2B ($ATG2B^{U2OS\text{-}KO}$) and ALIX ($ALIX^{HeLa\text{-}KO}$) cell lines by CRISPR/Cas9

Sequences of the two single-guide RNA (sgRNA) used to generate $ATG9A^{Huh7\text{-}KO}$ cells were GACCCCCAGGAGTGTGACGG and TCTGGAAACGGAGGATGCGG. Those to generate $ATG9A^{U2OS\text{-}KO}$, $ATG2A^{U2OS\text{-}KO}$ and $ATG2B^{U2OS\text{-}KO}$ were CTGTTGGTGCACGTCGCCGAGGG and CCCTGGGGGTGAATCACTATAGG, CACTGCACAGTGCGCGTGTCCGG and CCAGGGCACGGCCACCTCGATGG, and GAGGATTAGAAATGGTCTTCCGG and AAGAGCCCCATGGAACTGACAGG, respectively. The sequence of the sgRNA used to knockout ALIX (*PDCD6IP*) was CTTAAGTCGAGAGCCGACCG.

$ATG9A^{Huh7\text{-}KO}$ and $ALIX^{HeLa\text{-}KO}$ were generated by infecting target cells with the appropriate sgRNA, lentiviral vectors and lentiCRISPRv2 as previously described[64]. Briefly, HEK293T cells were transfected with lentiCRISPRv2 sgRNA vectors together with psPAX2 and pMD2.G at the ratio of 4 μg, 2.5 μg, and 1.5 μg/6-cm dish. 60 h later, the supernatants containing lentiviruses were collected and spun down at 300 g for 5 min to clear cell debris. Lentiviruses were diluted with DMEM full medium at 1:2 ratio and used to infect target cells overnight with the presence of 8 μg/ml of polybrene (hexadimethrine bromide) in 12-well plates. Then, the medium with lentivirus was removed and changed to fresh medium to continue incubation for 24 h. Cells were selected on 2 μg/ml puromycin for 5 days before validation of the knockout. Single clones were isolated by seeding single cells in 96-well plates after serial dilutions.

$ATG9A^{U2OS\text{-}KO}$, $ATG2A^{U2OS\text{-}KO}$ and $ATG2B^{U2OS\text{-}KO}$ were created by first cloning the sgRNA into the pX458 plasmid (Addgene), which also allow the simultaneous expression of Cas9 and GFP. U2OS were transfected with the generated plasmids using Xfect (Takara Bio), and 48 h later clonally sorted by FACS based on GFP expression. Single cell clones were then expanded, sequenced and protein expression was assessed by immunoblot.

Generating Flp-In cell lines

HEK293T Flp-In-FLAG-APEX2-ATG9A^{TetON} (HEK293T$^{APEX2\text{-}ATG9A}$) and HeLa Flp-In-mCherry-CHMP4A cell lines

HEK293T or HeLa Flp-In T-REX host cells were transfected with ATG9A and CHMP4A reconstructed plasmid, respectively, and the pOG44 expression plasmid at ratio of 9:1. 24 h after transfection, cells were washed and fresh medium added. One day later, cells were split into fresh medium containing 100 µg/ml hygromycin, at a confluency around 25%. Selective medium was renewed every 3–4 days until single cell clones could be identified. Hygromycin-resistant clones were picked and expanded. Clones were tested by immunoblotting, after overnight incubation in medium containing 1µg/ml tetracycline to analyze the expression of FLAG-APEX2-ATG9A or mCherry-CHMP4A.

Co-immunoprecipitations and immunoblotting

Cells transfected with 8-10 µg of plasmids were lysed in NP-40 buffer (ThermoFisher Scientific) supplemented with protease inhibitor cocktail (Roche) and 1 mM PMSF (Sigma) for 30 min on ice. Supernatants were incubated with 2-3 µg of antibodies at 4°C overnight. The immune complexes were captured with Dynabeads (ThermoFisher Scientific). Dynabeads were washed 3 times with PBS and bound proteins eluted with 2×Laemmli sample buffer (Bio-Rad), before to be subjected to immunoblot analysis. Immunoblotting images were visualized and analyzed using ImageLab v6.0.0.

Immunofluorescence confocal microscopy

For immunofluorescence confocal microscopy, cells were plated onto coverslips in 12 well plates. Cells were transfected with plasmids and treated as indicated in figures before being fixed in 4% paraformaldehyde for 10 min followed by permeabilization with PBS 0.1% saponin for 10 min. Cells were then blocked in PBS 5% BSA, 0.05% saponin for 30 min before primary antibodies labelling overnight at 4ºC. After washings with PBS and incubation with appropriate secondary antibodies for 1 h at room temperature, coverslips were mounted using ProLong Gold Antifade Mountant (Invitrogen) and analyzed by confocal microscopy using the Zeiss LSM510 Laser Scanning Microscope driven by Zeiss LSM 510 v4.2 SPI software.

GST pull-down Assay

Recombinant GST and GST-fusion proteins were produced in Escherichia coli SoluBL21 (Genlantis, #C700200) by inducing expression in overnight cultures with 50-75 µg/mL isopropyl β-D-1-thiogalactopyranoside (IPTG). Expressed proteins were purified by immobilization on Glutathione Sepharose 4 Fast Flow beads (GE Healthcare, #17-5132-01). For GST pull-down assays, myc-tagged proteins were in vitro translated and radiolabeled with [35S]-methionine using the TNT T7 Reticulocyte Lysate System (Promega, #l4610). Ten µL of in vitro translated proteins were precleared to reduce nonspecific binding with 10 µL of empty Glutathione Sepharose beads in 100 µL of NETN buffer (50 mM Tris pH 8.0, 150 mM NaCl, 1 mM EDTA, 0.5% NP-40) supplemented with cOmplete™ EDTA-free Protease Inhibitor Cocktail (Roche, #1183617001) for 30 min at 4 °C. This was followed by incubation with purified GST or GST-fusion proteins for 1-2h at 4 °C. The mixture was washed 5 times with NETN buffer by centrifugation at 2,500 g for 2 min followed by addition of 2XSDS gel-loading buffer (100 mM Tris pH 7.4, 4% SDS, 20% Glycerol, 0.2% Bromophenol blue and 200 mM dithiothreitol (DTT) (Sigma, #D0632)

and heating for 10 min. The proteins were then resolved by SDS-PAGE and the gel stained with Coomassie Brilliant Blue R-250 Dye (Thermo Fisher Scientific, #20278) to visualize the GST and GST-fusion proteins. The gel was vacuum-dried and radioactive signal detected by Bioimaging analyzer BAS-5000 (Fujifilm).

Plasma membrane damage

PM damage using the detergents digitonin and saponin was performed as described previously[6]. Briefly, 0.05% saponin or 50-200 µg/ml digitonin (as indicated) diluted in DMEM-10% FBS (complete medium) was applied to cells at 37°C for 1 min. Cells were then washed with complete media and fixed 3 min after the addition of detergents with 4% paraformaldehyde (PFA) in PBS or lysed.

PM damage using SLO was performed with a modified protocol[65]. Cells were washed with Ca^{2+}-free HBSS containing 5 mM EGTA at 37°C before to be washed twice in Ca^{2+}-free HBSS. Reduced SLO (10 mM DTT at room temperature for 5 min), was diluted in Ca^{2+}-free HBSS (200 U/mL) and added on target cells for 10 min at 37°C. Cells were washed in complete media before to be fixed or lysed.

PM damage induced by GBI was performed as described previously[66]. Acid-washed glass beads were gently poured over the cells (~35 mg of beads per well for a 24-w plate). The beads were agitated over the cells for 1 min on a rotator platform at 160 rpm. Thirty seconds after GBI, the cells were washed with warm PBS and fixed or lysed.

PM damage induced by the pore-forming FLAG-GSDMD-NT fragment was performed as described previously[67]. Huh7 cells were transfected with 100 ng/10^5 cells of FLAG-GSDMD-NT plasmid (Addgene #80951), FLAG-GSDMD (Addgene #80950) or FLAG-GSDMD-NT-4A (Addgene #80952) using lipofectine 2000 in OptiMEM for 2 h. Then, cells were washed in complete media before assessing PI uptake and cell viability (Live/Dead, Thermo Scientific) at the indicated time points.

PM damage triggered by cleavage of endogenous GSDMD was performed as described previously for BMMs and human cell lines[8 29]. BMMs were seeded at a density of 3.10^4 cells per well in 96-well plate 1 day prior to stimulation, and grown overnight at 37°C in 5% CO_2. The next day, supernatant was removed and BMMs were primed for 4 h with 50 ng/well of lipopolysaccharyde (LPS) O55:B5. Then, 3.10^4 cells were transfected with LPS complexes prepared by mixing 100 µl of OptiMEM with ultrapure LPS O111:B4 (Invivogen) and 0.5 µl of lipofectamine RNAiMAX (Thermo Scientific). The transfection mixture was incubated for 10 min at room temperature and subsequently added to the cells. Plates were centrifuged at 1,000 rpm for 5 min at 37°C. BMMs were incubated for the indicated times at 37°C in 5% CO_2 before to measure PM damage using the PI assay and the LDH release in the supernatant (Promega, G1780). For U2OS cells, 2 µg of LPS O111:B4 (Invivogen) was mixed with 2.10^6 U2OS cells in 100 µl of Amaxa Nucleofector® Kit V buffer (Lonza, VVCA-1003) and electroporated according to manufacturer's instructions. Cells were then plated in 96-well plate for 6 h or 17 h before measuring LDH release in the supernatant and perform the PI assay.

Plasma membrane leakage induced by SARS-CoV-2 ORF3a was performed by transfection of ORF3a (FLAG or GFP tagged in Nter) using lipofectine 2000 in OptiMEM for 2 h. Then, cells were washed in complete media before assessing PI uptake the next day. This plasmid was obtained by LR cloning reaction (Gateway, ThermoFisher) in

pDEST-FLAG or pDEST-GFP vector using pDONR207 SARS-Cov-2 ORF3a (Addgene, #141271).

Plasma membrane permeabilization assays

For the PI assay, cells were incubated with 100 µg/ml propidium iodide diluted in complete media for 1 min at 37°C, 2 min after the addition of saponin or digitonin, 10 min after SLO or 1 min after GBI treatment. After propidium iodide incubation, cells were fixed with 4% PFA.

For the Dextran-10k (Dx-10) staining, cells were incubated for 1 min at 37°C with 500 µg/ml of Dx-10 diluted in complete media, 2 min after the addition of digitonin and before 4% PFA fixation.

PMHAL Assay

Huh7 cells were transiently transfected with the HaloTag (HT) probe (PEX3-GFP-HT) before digitonin treatment for 1 min. Cells were then washed for 1 min in complete media before incubation with complete media containing the HT ligands MIL and/or MPL (1:1000) for 1 min before 4% PFA fixation and Hoechst staining. For HCM quantification, cells transfected with the PEX3-GFP-HT probe were gated using GFP total cell fluorescence intensity. A mask was then assigned to GFP+ puncta according to fluorescence intensity and puncta area. The same threshold was applied to $ATG9A^{WT}$ and $ATG9A^{KO}$ cells. The fluorescence intensity of MIL or MPL colocalizing with GFP-HT puncta masks (GFP+MIL+ or GFP+MPL+, respectively) was then assessed.

Endocytosis assay

To monitor endocytosis, we used DQ-Red BSA as a fluid phase tracer. Cells were incubated with 10 µg/ml of DQ-Red BSA diluted in complete media for 2 min at 37°C after digitonin treatment. Endocytosis was stopped by 4% PFA fixation.

Bimolecular fluorescence complementation assay

HeLa cells were transiently transfected with pDEST-VN^{ALIX} and pDEST-VC^{ATG9A} before to analyze Venus fluorescence was analyzed by HCM and confocal microscopy.

Cell surface biotinylation

ATG9A cell surface biotinylation was performed as described previously[23], with an adapted protocol suitable for the analysis of proteins during PM damage[66]. HEK293T cells transiently expressing GFP-ATG9A were treated with PM damage agents (digitonin, SLO or GBI) or EBSS for 1h. Cells were rinsed twice with ice-cold PBS^{2+} (PBS containing 1 mM $MgCl_2$ and 0.1 mM $CaCl_2$) and were subsequently incubated with freshly prepared ice-cold 0.4 mM maleimide-PEG_2-biotin (ThermoFisher Scientifc) in PBS, 1 mM $MgCl_2$, 2 mM $CaCl_2$, 150 mM NaCl, for 60 min at 4°C with gentle agitation. Unreacted maleimide-PEG_2-biotin was then quenched by washing the cells twice with ice-cold quenching buffer (PBS, 1 mM $MgCl_2$, 0.1 mM $CaCl_2$, 100 mM glycine) for 20 min at 4°C. Cells were subsequently rinsed twice with ice-cold PBS^{2+} and scraped in NP-40 buffer (50 mM Tris-HCl, pH 8, 150 mM NaCl, 1% NP-40 and supplemented with protease inhibitor cocktails). After 30 min on ice, lysates were cleared by centrifugation at 16,000 g for 10 min at 4°C, and protein concentration determined using the BCA protein assay (Pierce). 4 mg of

proteins were incubated with 3 µg of GFP antibody overnight at 4°C. The immune complexes were captured with Dynabeads (ThermoFisher Scientific). The Dynabeads were wash with PBS three times and bound proteins eluted with 2×Laemmli sample buffer (Bio-Rad), before to be analyzed by immunoblot using an HRP-conjugated streptavidin antibody.

hEGF treatment

Cells were washed three times with pre-warmed PBS and serum-starved with DMEM containing 0.1% FBS for HeLa or serum-free DMEM for U2OS cells. After 24h of starvation, cells were stimulated during 30 min with hEGF in DMEM (50 ng/mL for HeLa and 100 ng/mL for U2OS).

N-ethylmaleimide (NEM) treatment

NEM treatment was performed as previously described[68]. Cells were washed twice in PBS supplemented with 0.1 mM $CaCl_2$ and 0.1 mM $MgCl_2$ (PBS^+) and then treated in PBS^+ on ice either with 1 mM NEM for 15 min followed by quenching with 2 mM DTT for 15 min, or with 1 mM NEM plus 2 mM DTT for 30 min. Finally, cells were washed in PBS^+ and incubated in complete medium for 30 min at 37°C before inducing PM damage.

Extracellular vesicles (EVs) enrichment and analysis

$ATG9A^{Huh7\text{-}KO}$ and their parental $ATG9A^{Huh7\text{-}WT}$ cells were treated with 100 µg/ml digitonin diluted in OptiMEM for 1 min. Cells were washed two times with OptiMEM and the supernatant containing the released EVs was harvested 5 min after digitonin addition. EVs were isolated using the Total exosome isolation reagent (ThermoFisher Scientific), according to the manufacturer's instructions. The obtained cell pellets were suspended in 100 µl of PBS and analyzed by immunoblotting or in a nanoparticle tracking instrument.
Isolated EVs (as described above) from the $ATG9A^{Huh7\text{-}KO}$ and their parental $ATG9A^{Huh7\text{-}WT}$ cell culture supernatant were diluted in PBS and used for nanoparticle tracking analysis using a Nanosight NS300 instrument (NanoSight Ltd.), followed by evaluation using the Nanoparticle Tracking Analysis (NTA) software. Conditions were as follows: camera type, sCMOS; detection threshold, 2; recording of 800 frames/sample at 25 frames/s.

Nanoparticle tracking analysis

Isolated EVs (as described above) from the Huh7 $ATG9A^{KO}$ and their parental Huh7 $ATG9A^{WT}$ cell culture supernatants were diluted in PBS and used for nanoparticle tracking analysis using a Nanosight NS300 instrument (NanoSight Ltd.), followed by evaluation using the Nanoparticle Tracking Analysis (NTA) software. Conditions were as follows: camera type, sCMOS; detection threshold, 2; recording for 800 frames at 25 frames/s.

Plasma membrane damage by mycobacteria

Mycobacterium tuberculosis Erdman (Erdman) culture was prepared by thawing frozen stock aliquot and grown in 7H9 Middlebrook liquid medium supplemented with oleic acid, albumin, dextrose and catalase (OADC, Becton Dickinson, Inc., Sparks, MD, USA), 0.5% glycerol and 0.05% Tween-80. Cultures were grown at 37°C. $ATG9A^{Huh7\text{-}KO}$ and their parental $ATG9A^{Huh7\text{-}WT}$ cells were co-incubated with Mtb Erdman at MOI 5 or 10 (or *Mycobacterium bovis* BCG at MOI 10) for 1 h following with PI staining (100 µg/mL in complete media) and fixation in 4% PFA for 1h to analyze PM permeability using HCM.

High content microscopy (HCM)

Cells in 96 well plates were treated as indicated in each experiment before to be fixed in 4% PFA. Cells were then permeabilized with 0.1% saponin in 3% bovine serum albumin (BSA) for 30 min followed by incubation with primary antibodies overnight at 4°C and secondary antibodies for 1h at room temperature. High-content microscopy with automated image acquisition and quantification was carried out using a Cellomics HCS scanner and iDEV software (ThermoFisher Scientific). Automated epifluorescence image collection was performed using a minimum of 500 cells per well and ≥ 5 wells/sample. Epifluorescence images were machine analyzed using preset scanning parameters and object mask definitions. Hoechst 33342 staining was used for autofocus and to automatically define cellular outlines based on background staining of the cytoplasm. Primary objects (cells, regions of interests (ROI) or targets) were algorithm-defined for shape/segmentation, maximum/minimum average intensity, total area and total intensity minimum and maximum limits, etc., to automatically identify puncta or other profiles within valid primary objects. Nuclei were defined as a ROI for propidium iodide staining. All data collection, processing (object, ROI and target mask assignments) and analyses were computer-driven independently of human operators.

TIRF dSTORM super-resolution imaging and analysis

Super-resolution imaging by dSTORM TIRF and data analysis were done as described previously[69]. HeLa cells transiently transfected with FLAG-ATG9A and MyrPalm-EGFP were plated on 25 mm round #1.5 coverslips (Warner Instruments) coated with Poly-L-lysine solution (Sigma-Aldrich) and allowed to adhere overnight. After two steps fixation (first step (0.6% PFA, 0.1% Glutaraldehyde (GA), 0.1% saponin) for 60 s; second step (4% PFA, 0.2% GA) for 3 h), cells were washed by 1xPBS twice, and incubated with 0.1% $NaBH_4$ for 5 min. After two washes with PBS, cells were incubated with 10 mM Tris-HCl, pH 7.5 for 5 min and blocked with 5% BSA containing 0.05% saponin for 15 min. After a wash with PBS, cells were incubated with anti-FLAG antibody overnight at 4°C and washed with PBS three times followed by labeling with Alexa Fluor 647 (A21245, Invitrogen). The coverslip was mounted on an Attofluor cell chamber (A-7816, ThermoFisher Scientific) with 1.1 ml of Imaging buffer (50 mM Tris-HCl, pH 8, 10 mM NaCl, 10% glucose, 168.8 U/ml glucose oxidase (Sigma), 1,404 U/ml catalase (Sigma), 20 mM 2-aminoethanethiol). The chamber was sealed by placing an additional coverslip over the chamber, and the oxygen-scavenging reaction in the Imaging buffer was allowed to proceed for 20 min at room temperature before starting the imaging.

Imaging was performed using a custom-built TIRF illuminating fluorescence microscope controlled by custom-written software (github.com/LidkeLab/matlab-instrument-control) in MATLAB (MathWorks Inc.). The samples were loaded on an xyz piezo stage (Mad City Labs, Nano-LPS100) mounted on a manual x-y translator. Images were recorded on an iXon 897 electron-multiplying charge coupled (EMCCD) camera (Andor Technologies, South Windsor, CT). The EMCCD gain was set to 100, and 256x256 pixel frames were collected with a pixel resolution of 0.1078 µm. A 642-nm laser (collimated from a laser diode, HL6366DG, Thorlabs) was used for sample excitation. The laser was coupled into a multi-mode fiber (P1-488PM-FC-2, Thorlabs) and focused onto the back focal plane of the objective lens (UAPON 150XOTIRF, Olympus America Inc.).

Optimal laser penetration depth was achieved by adjusting the TIRF angle, translating the laser beam away from the optical axis along the back focal plane of the objective. Sample excitation was done through a quad-band dichroic and filter set (LF405/488/561/635-A; Semrock, Rochester, NY). Fluorescence emission path included a band-pass filter (685/45, Brightline) and a quadband optical filter (Photometrics, QV2-SQ) with 4 filter sets (600/37,525/45,685/40,445/45, Brightline).

When imaging the first signal, for each target cell a brightfield reference image was saved in addition to the x-y stage position coordinates. The 642-nm laser was used at ~1 kW/cm^2 to take 20 sets of 2,000 frames (a total of 40,000) at 60 Hz. After imaging all target cells, the Imaging buffer was replaced with PBS, the residual fluorescence was photobleached and quenched with $NaBH_4$, and the preparation washed twice with PBS. Before the second round of imaging, cells were blocked for 30 min, labeled with anti-GFP antibody coupled with Alexa Fluor 647 (A-31852, ThermoFisher Scientifc) at 1:500 for 1h and washed with PBS three times. Before the second round of imaging, each target cell was located and realigned using the saved brightfield reference image as described in [70].

Data were analyzed via a 2D localization algorithm based on maximum likelihood estimation[71]. The localized emitters were filtered through thresholds of maximum background photon counts of 200, minimum photon counts per frame per emitter of 250, and a data model hypothesis test [72] with a minimum p-value of 0.01. The accepted emitters were used to reconstruct the super-resolution image. Each emitter was represented by a 2D Gaussian function with σx and σy equal to the localization precisions, which were calculated from the Cramér-Rao Lower Bound (CRLB). Clustering analysis was performed with MATLAB code using clustering tools (http://stmc.health.unm.edu/tools-and-data/). ROI were selected from the image. Clustering was then performed separately for each label in each ROI, using the density-based DBSCAN algorithm choosing a maximal nearest neighbor distance of 40 nm and requiring clusters to contain at least 5 observations. In all cases, most observations for each label in each ROI formed a single cluster. Cluster boundaries were produced via the MATLAB “boundary” function, from which inter-label cluster distances were computed.

Photodamage and time-lapse imaging

For laser-induced PM damage, Huh7 cells transiently transfected with GFP-ATG9A using lipofectamine 2000, were plated in a chambered coverslip (µ- Slide 8 well, ibiTreat, #80826) and allowed to adhere overnight. Cells were maintained at 37°C with a supply of 5% CO_2. Cells were incubated with medium containing 160 µg/ml propidium iodide right before photodamage. Photodamage and associated time-lapse acquisitions were performed with a Leica TCS SP8 confocal microscope equipped with a 405 laser (100 mW, set at 100%, 50 iterations) to induce PM damage. The acquisition was performed with a 63X/1.4NA oil immersion apochromat objective and the resulting images (1 image/0.8 sec) were processed with Leica software LAS AF, Adobe After Effects and Adobe Premiere Pro.

TIRF microscopy

Total internal reflection fluorescence (TIRF) images were obtained using a 100X/1,49NA oil immersion objective and a TIRF module built-in Eclipse TI-E inverted microscope (Nikon Instruments Inc.). A 488-nm laser and a 543-nm laser were used for excitation,

and emission signals were filtered with 528 ± 19-nm and 617 ± 36-nm band-pass filters for Alexa Fluor 488 and Alexa Fluor 555 imaging, respectively. Images were collected by a QuantEM 512SC Imaging Camera (Photometrics) operated with NIS-Elements software (Nikon Instruments Inc.). For puncta counting, images were converted to binary images by thresholding using ImageJ (National Institutes of Health).

Plasma membrane tension measurement

ATG9A^{WT} or ATG9A^{KO} Huh7 cells were spread at around 70 % confluence on a 8 well glass bottom microslides (Ibidi, #80826) and grew in DMEM medium supplemented with 10% FBS for 24 h. The medium was replaced with the same medium containing 2 µM of Flipper-TR® probe (SC020, Spirochrome) and kept for at least 30 min before imaging. FLIM imaging was performed using a Leica TCS SP8 SMD microscope equipped with a time-correlated single-photon counting module from PicoQuant58. Excitation was performed using a pulsed 470 nm laser (PicoQuant, LDH-D-C-470) operating at 40 MHz, and the emission signal was collected through a 600/50 nm bandpass filter using a MPD-SPAD detector (Micro Photon Devices - Single Photon Avalanche Diode) and a TimeHarp 260 PICO board (PicoQuant). SymPhoTime software (PicoQuant) was then used to fit fluorescence decay data (from full images) to a dual exponential model.

Cell fixation, DAB reaction, embedding and electron microscopy analyses

HEK293T$^{APEX2\text{-}ATG9A}$ cells were exposed or not with 50 µg/ml of digitonin, for 1 min before to be fixed and carry out 3,3'-diaminobenzidine (DAB oxidation reaction as previously described[73]. Briefly, an equal volume of double strength fixative (4% glutaraldehyde (GA) in 0.1 M sodium cacodylate buffer, pH 7.4) was added to the cells for 20 min at room temperature, prior to fixing the cells with one volume of single strength fixative (2% glutaraldehyde in 0.1 M sodium cacodylate buffer, pH 7.4) at 4°C for 1 h. After 5 washes with cacodylate buffer (pH 7.4) followed by 5 washes in PBS, a filtered solution of 0.5 mg/ml DAB (Sigma) in PBS was mixed (10'0000:3) with 30% H_2O_2 (Sigma) and added to the cells for 7 min. The DAB oxidation reaction was monitored using a bright field microscope and stopped by rinsing the cells 3 times with PBS for 5 min. Cells were then processed for EM by embedding them in EPON resin as previously described[74]. Ultra-thin 70-nm sections were cut using a Leica EM UC7 ultramicrotome (Leica Microsystems) and collected at 150 formvar-mesh copper grids. Cell sections were examined using a CM100bio TEM (FEI). The quantification of ATG9A at the plasma membrane was performed on APEX2-ATG9A-positive cell profiles per condition in the following way: The entire length of the plasma membrane as well as the sections of the plasma membrane stained with diaminobenzidine in each cell profile were measured with the Image J software. The average percentage of the plasma membrane positive for APEX2-ATG9A in 45 randomly selected cell profiles were analyzed.

APEX2-labeling and streptavidin enrichment for LC-MS/MS analysis

HEK293T$^{APEX2\text{-}ATG9A}$ cells were incubated in 500 µM biotin-phenol (AdipoGen) in complete media before inducing plasma membrane damage. For digitonin treatment, 100 µg/ml digitonin diluted in complete media was added on the cells for 1 min. Cells were washed once in complete media before adding back biotin-phenol media. For SLO treatment, cells were washed at 37°C with Ca^{2+}-free HBSS containing 5 mM EGTA

followed by two more washes in Ca^{2+}-free HBSS. SLO was reduced by 10 mM DTT 5 min at room temperature before dilution in Ca^{2+}-free HBSS (200 U/ml) and added on target cells for 10 min at 37°C. Cells were then washed once in complete media before adding biotin-phenol media. For GBI treatment, ~1.6 g of beads were gently poured on the 10 cm petri dish containing the cells. The beads were agitated over the cells for 1 min on a rotator platform at 160 rpm. A 1 min pulse with 1 mM H_2O_2 at room temperature was stopped with quenching buffer (10 mM sodium ascorbate, 10 mM sodium azide and 5 mM Trolox in PBS. All samples were washed twice with quenching buffer, and twice with PBS.

For LC-MS/MS analysis, cells pellets were lysed in 500 µl ice-cold lysis buffer (6 M urea, 0.3 M NaCl, 1 mM EDTA, 1 mM EGTA, 10 mM sodium ascorbate, 10 mM sodium azide, 5 mM Trolox, 1% glycerol and 25 mm Tris-HCl, pH 7.5) for 30 min by gentle pipetting. Lysates were clarified by centrifugation and protein concentrations determined using Pierce 660 nm protein assay reagent. Streptavidin–coated magnetic beads (Pierce) were washed with lysis buffer. 1 mg of each sample was mixed with 100 µl of streptavidin beads. The suspensions were gently rotated at 4°C for overnight to bind biotinylated proteins. The flow-through after enrichment was removed and the beads were washed in sequence with 1 ml IP buffer (150 mM NaCl, 10 mM Tris-HCl, pH 8.0, 1 mM EDTA, 1 mM EGTA, 1% Triton X-100) twice*;* 1 ml 1M KCl; 1ml of 50 mM Na_2CO_3; 1 ml 2 M urea in 20 mM Tris HCl, pH 8.0; and 1 ml IP buffer. Biotinylated proteins were eluted, 10% of the sample *processed* for immunoblotting and 90% of the sample processed for mass spectrometry.

LC-MS/MS

Digested peptides were analyzed by LC-MS/MS on a Thermo Scientific Q Exactive Plus Orbitrap Mass spectrometer in conjunction Proxeon Easy-nLC II HPLC (Thermo Scientific) and Proxeon nanospray source. The digested peptides were loaded a 100 micron x 25 mm Magic C18 100Å 5U reverse phase trap where they were desalted online before being separated using a 75 micron x 150 mm Magic C18 200Å 3U reverse phase column. Peptides were eluted using a 140 min gradient with a flow rate of 300 nl/min. A MS survey scan was obtained for the m/z range 350-1600, MS/MS spectra were acquired using a top 15 method, where the top 15 ions in the MS spectra were subjected to HCD (High Energy Collisional Dissociation). An isolation mass window of 1.6 m/z was for the precursor ion selection, and normalized collision energy of 27% was used for fragmentation. A 15 s duration was used for the dynamic exclusion.

Mass spectrometry data processing and analysis

Tandem mass spectra were extracted by Proteome Discoverer version 2.2. Charge state deconvolution and deisotoping were not performed. All MS/MS samples were analyzed using X! Tandem (The GPM, thegpm.org; version X! Tandem Alanine (2017.2.1.4)). X! Tandem was set up to search the Uniprot Human proteome database plus 110 common laboratory contaminants and an equal number of decoy sequences (147936 entries total) assuming the digestion enzyme trypsin. X! Tandem was searched with a fragment ion mass tolerance of 20 PPM and a parent ion tolerance of 20 PPM. Glu->pyro-Glu of the n-terminus, ammonia-loss of the n-terminus, gln->pyro-Glu of the n-terminus, deamidated

of asparagine and glutamine, oxidation of methionine and tryptophan and dioxidation of methionine and tryptophan were specified in X! Tandem as variable modifications.

Scaffold (version Scaffold_4.9.0, Proteome Software Inc., Portland, OR) was used to validate MS/MS based peptide and protein identifications. Peptide identifications were accepted if they could be established at greater than 98.0% probability by the Scaffold Local FDR algorithm. Peptide identifications were also required to exceed specific database search engine thresholds. X! Tandem identifications required at least -log(E-Value) of 2. Protein identifications were accepted if they could be established at greater than 5.0% probability to achieve an FDR less than 5.0% and contained at least 1 identified peptide. This resulted in a Peptide decoy FDR of 0.7% and a Protein Decoy FDR of 0.66%. Proteins that contained similar peptides and could not be differentiated based on MS/MS analysis alone were grouped to satisfy the principles of parsimony. Proteins sharing significant peptide evidence were grouped into clusters. Raw data, and Scaffold results are available from the MassIVE proteomics repository (MSV000084519) and Proteome Exchange PXD016084.

BioWeB assay: APEX2-labeling and streptavidin enrichment for immunoblotting analyses

HEK293T$^{APEX2\text{-}ATG9A}$ cells were treated as described above for LC-MS/MS analysis. Cells were lysed in 500 µl of ice-cold NP-40 buffer for 30 min on ice. Lysates were clarified by centrifugation and protein concentrations determined using Pierce 660 nm protein assay reagent. One mg of each sample was mixed with 100 µl of streptavidin magnetic beads (Pierce). The suspensions were gently rotated at 4°C overnight to bind biotinylated proteins. The flow-through after enrichment was removed and the beads were washed in sequence with 1 ml IP buffer twice; 1 ml 1M KCl; 1ml of 50 mM Na_2CO_3; 1 ml 2M urea in 20 mM Tris-HCl, pH8; and 1 ml IP buffer. Biotinylated proteins were eluted with 2×Laemmli sample buffer (Bio-Rad) and subjected to immunoblot analysis.

Statistics and Reproducibility

Data in this paper are presented as means±SEM (n ≥ 3). Data were analyzed with either analysis of variance (ANOVA) with Dunnett's, Tukey's or Sidak's HSD post-hoc test, or unpaired student's *t* test using GraphPad Prism v7 to determine statistical significance. No statistical methods were used to predetermine the sample sizes. The number of independent samples and any statistical tests used are indicated in the figure legends, and all the replicates reproduced the shown findings. The experiments were repeated at least 3 times wherever representative results are shown.

Data availability

Mass spectrometry raw data and Scaffold results have been deposited in the MassIVE proteomics repository (MSV000084519) (https://massive.ucsd.edu) and Proteome Xchange with the primary accession code PXD016084 (http://www.proteomexchange.org). Source data have been provided in Source Data. All other data supporting the findings of this study are available from the corresponding author on reasonable request.

Code availability

TIRF-SR Imaging was performed using a custom-built TIRF illuminating fluorescence microscope controlled by a custom-written software (github.com/LidkeLab/matlab-instrument-control) in MATLAB (MathWorks Inc.).

References

63. Yamaguchi, J. *et al.* Atg9a deficiency causes axon-specific lesions including neuronal circuit dysgenesis. *Autophagy* **14**, 764-777 (2018).
64. Sanjana, N.E., Shalem, O. & Zhang, F. Improved vectors and genome-wide libraries for CRISPR screening. *Nat Methods* **11**, 783-784 (2014).
65. Idone, V. *et al.* Repair of injured plasma membrane by rapid Ca2+-dependent endocytosis. *J Cell Biol* **180**, 905-914 (2008).
66. Mellgren, R.L. A plasma membrane wound proteome: reversible externalization of intracellular proteins following reparable mechanical damage. *J Biol Chem* **285**, 36597-36607 (2010).
67. Liu, X. *et al.* Inflammasome-activated gasdermin D causes pyroptosis by forming membrane pores. *Nature* **535**, 153-158 (2016).
68. Galli, T. *et al.* A novel tetanus neurotoxin-insensitive vesicle-associated membrane protein in SNARE complexes of the apical plasma membrane of epithelial cells. *Mol Biol Cell* **9**, 1437-1448 (1998).
69. Pallikkuth, S. *et al.* Sequential super-resolution imaging using DNA strand displacement. *PLoS One* **13**, e0203291 (2018).
70. Valley, C.C., Liu, S., Lidke, D.S. & Lidke, K.A. Sequential superresolution imaging of multiple targets using a single fluorophore. *PLoS One* **10**, e0123941 (2015).
71. Smith, C.S., Joseph, N., Rieger, B. & Lidke, K.A. Fast, single-molecule localization that achieves theoretically minimum uncertainty. *Nat Methods* **7**, 373-375 (2010).
72. Huang, F., Schwartz, S.L., Byars, J.M. & Lidke, K.A. Simultaneous multiple-emitter fitting for single molecule super-resolution imaging. *Biomed Opt Express* **2**, 1377-1393 (2011).
73. Martell, J.D., Deerinck, T.J., Lam, S.S., Ellisman, M.H. & Ting, A.Y. Electron microscopy using the genetically encoded APEX2 tag in cultured mammalian cells. *Nat Protoc* **12**, 1792-1816 (2017).
74. Zhou, X. *et al.* Ultrastructural Characterization of Membrane Rearrangements Induced by Porcine Epidemic Diarrhea Virus Infection. *Viruses* **9** (2017).

Ext Data Fig1

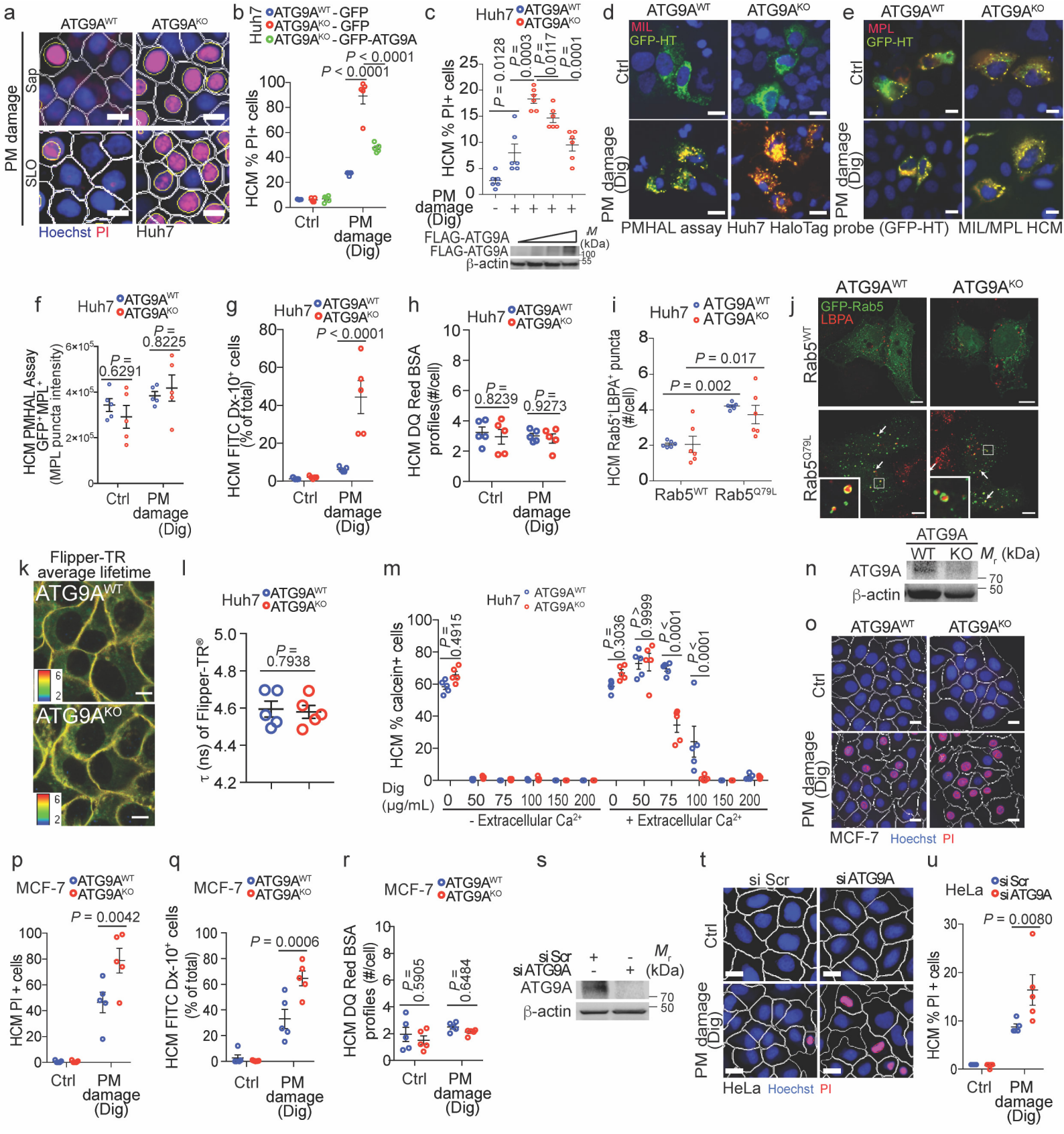

Ext Data Fig2

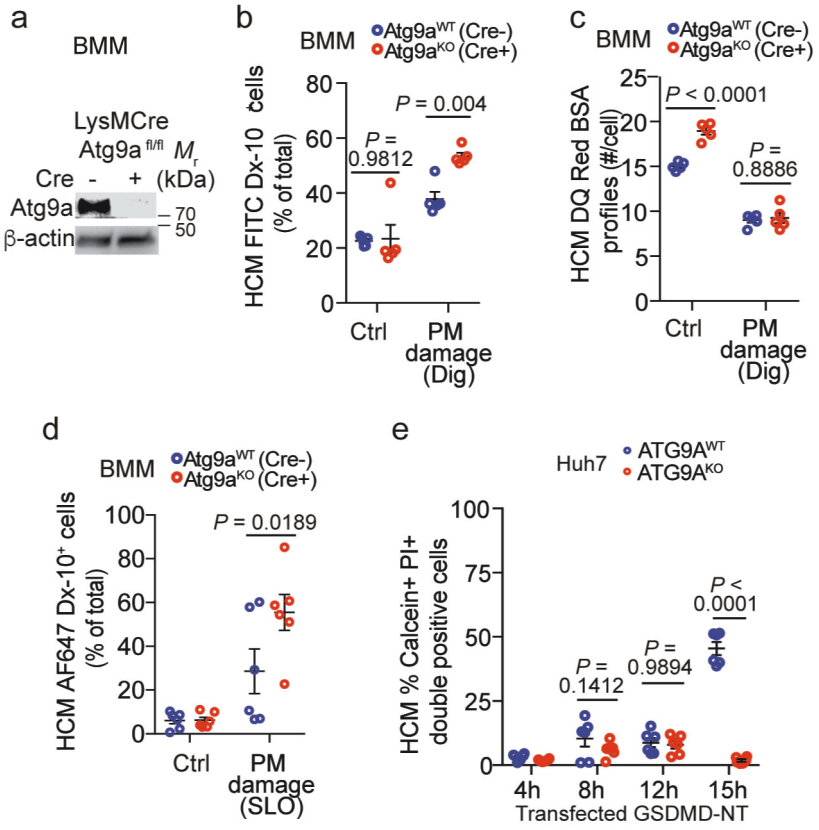

Ext Data Fig3

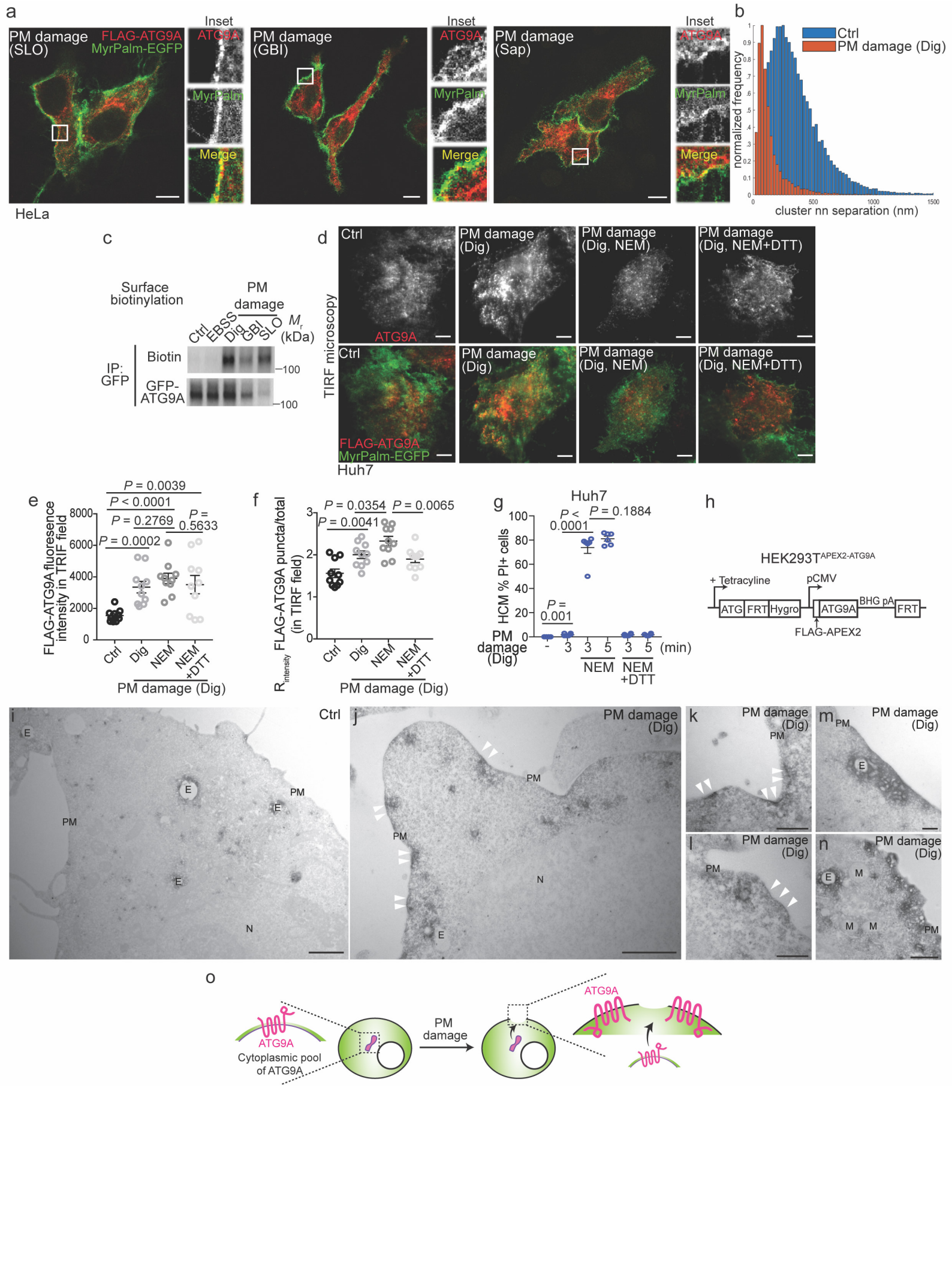

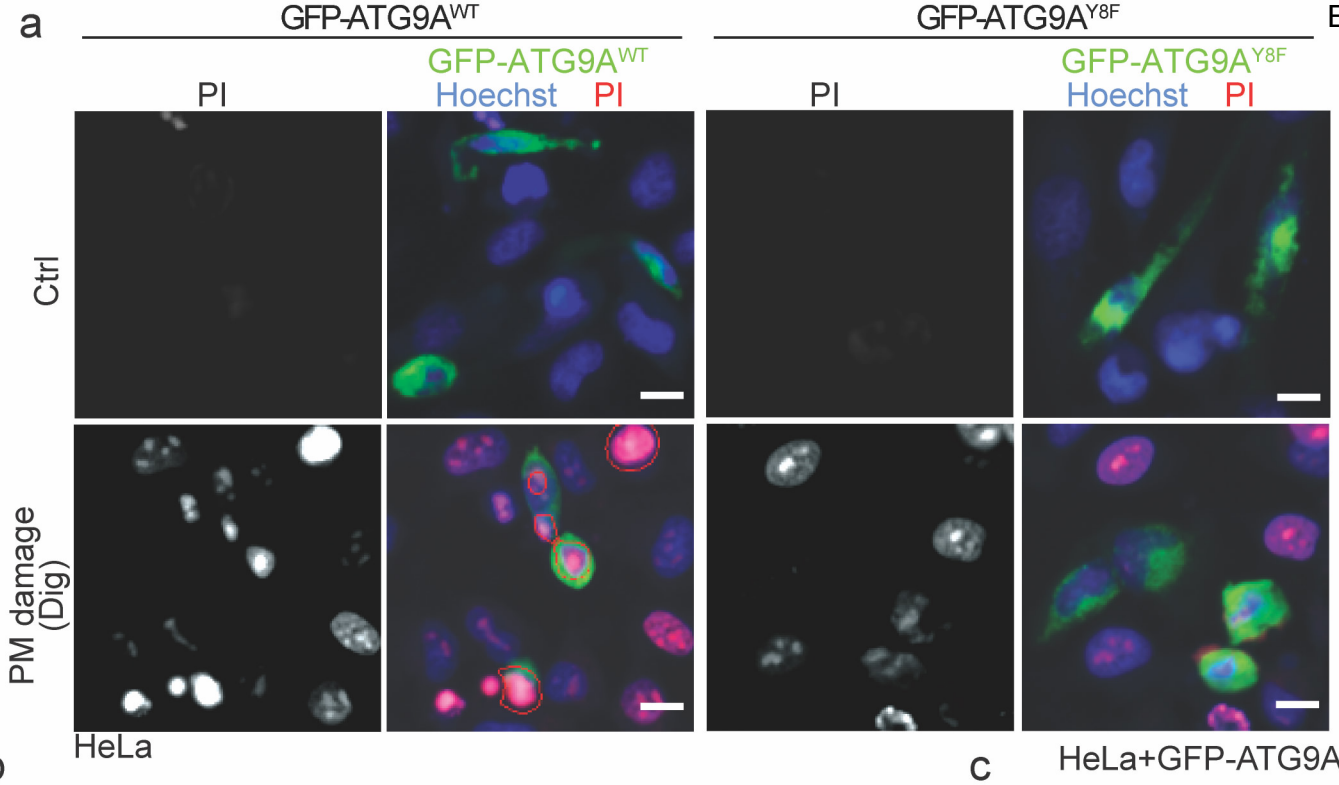
a
GFP-ATG9A^WT
GFP-ATG9A^Y8F
PI
GFP-ATG9A^WT
Hoechst PI
PI
GFP-ATG9A^Y8F
Hoechst PI
Ctrl
PM damage (Dig)
HeLa

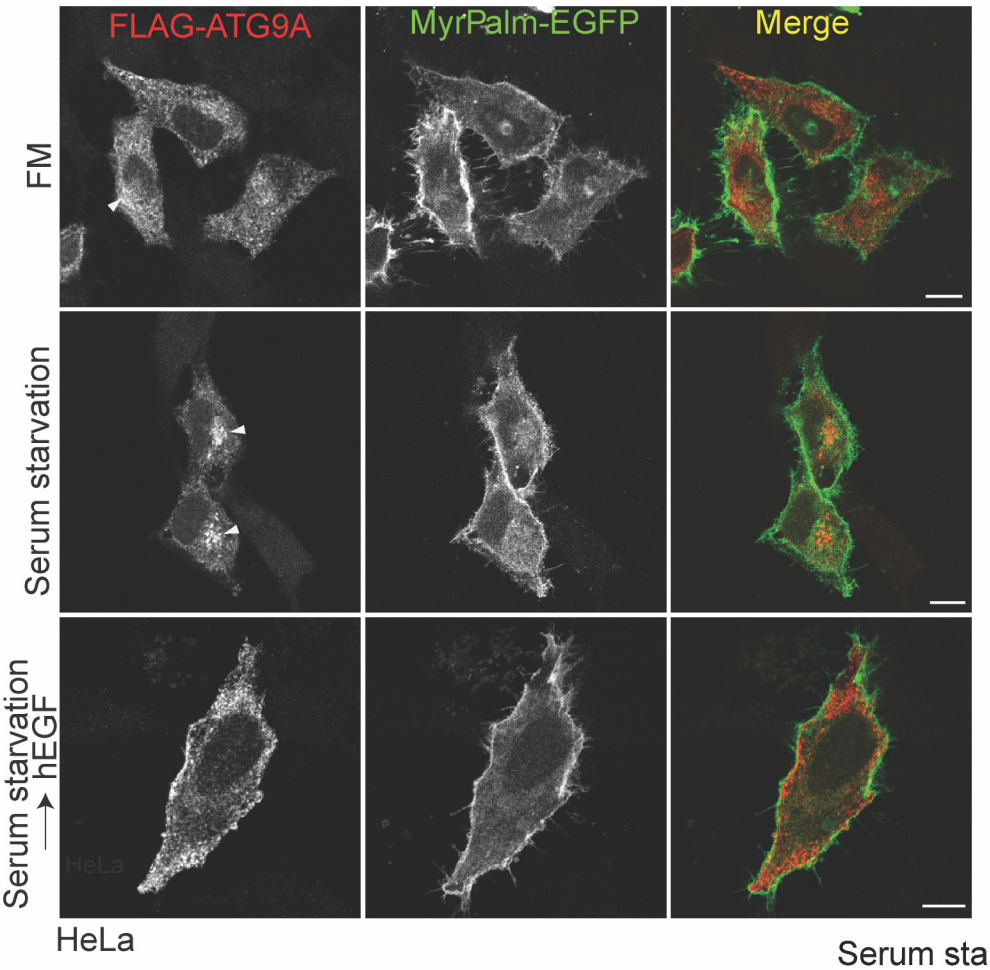
b
FLAG-ATG9A
MyrPalm-EGFP
Merge
FM
Serum starvation
Serum starvation → hEGF
HeLa

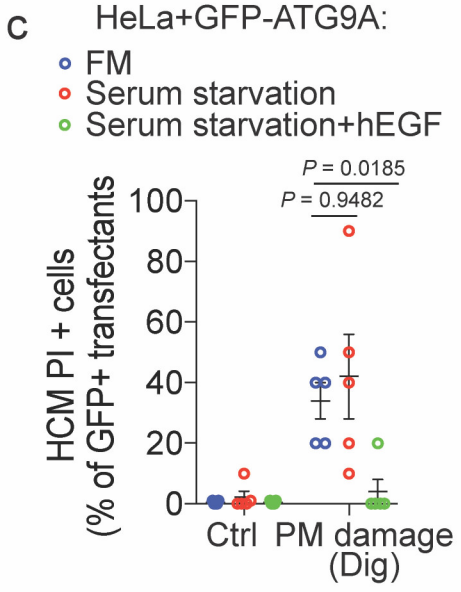
c
HeLa+GFP-ATG9A:
FM
Serum starvation
Serum starvation+hEGF
HCM PI + cells (% of GFP+ transfectants
P = 0.0185
P = 0.9482
Ctrl
PM damage (Dig)

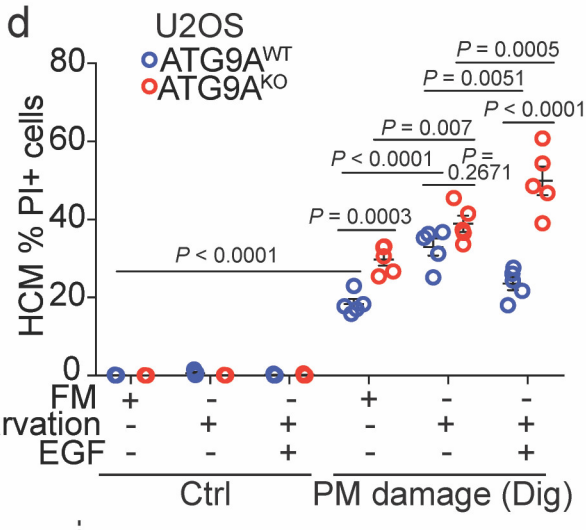
d
U2OS
ATG9A^WT
ATG9A^KO
HCM % PI+ cells
P = 0.0005
P = 0.0051
P < 0.0001
P = 0.007
P < 0.0001
P = 0.2671
P = 0.0003
P < 0.0001
FM
Serum starvation
EGF
Ctrl
PM damage (Dig)

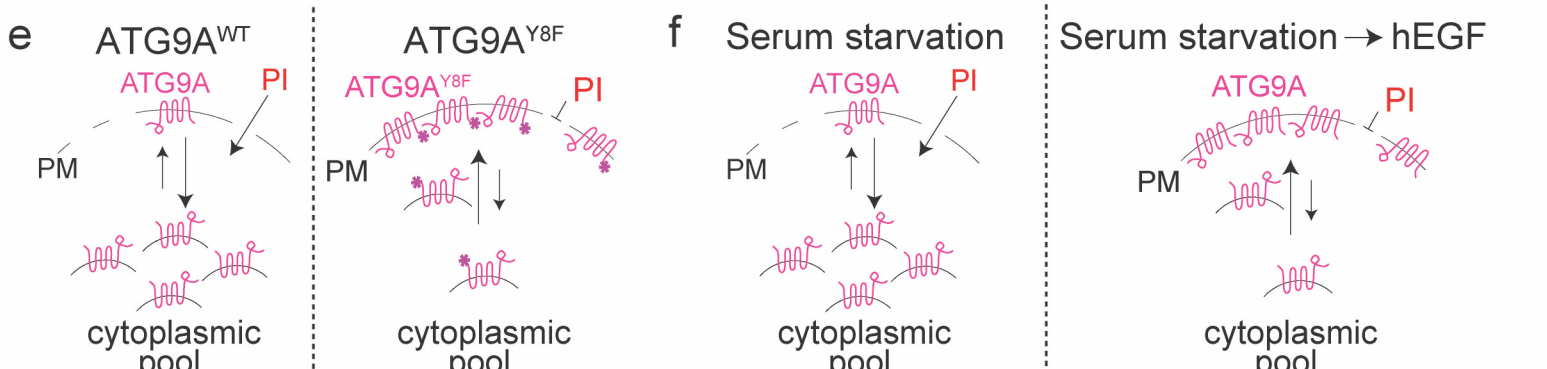
e
ATG9A^WT
ATG9A
PI
PM
cytoplasmic pool
ATG9A^Y8F
ATG9A^Y8F
PI
PM
cytoplasmic pool
f
Serum starvation
ATG9A
PI
PM
cytoplasmic pool
Serum starvation → hEGF
ATG9A
PI
PM
cytoplasmic pool

Ext Data Fig5

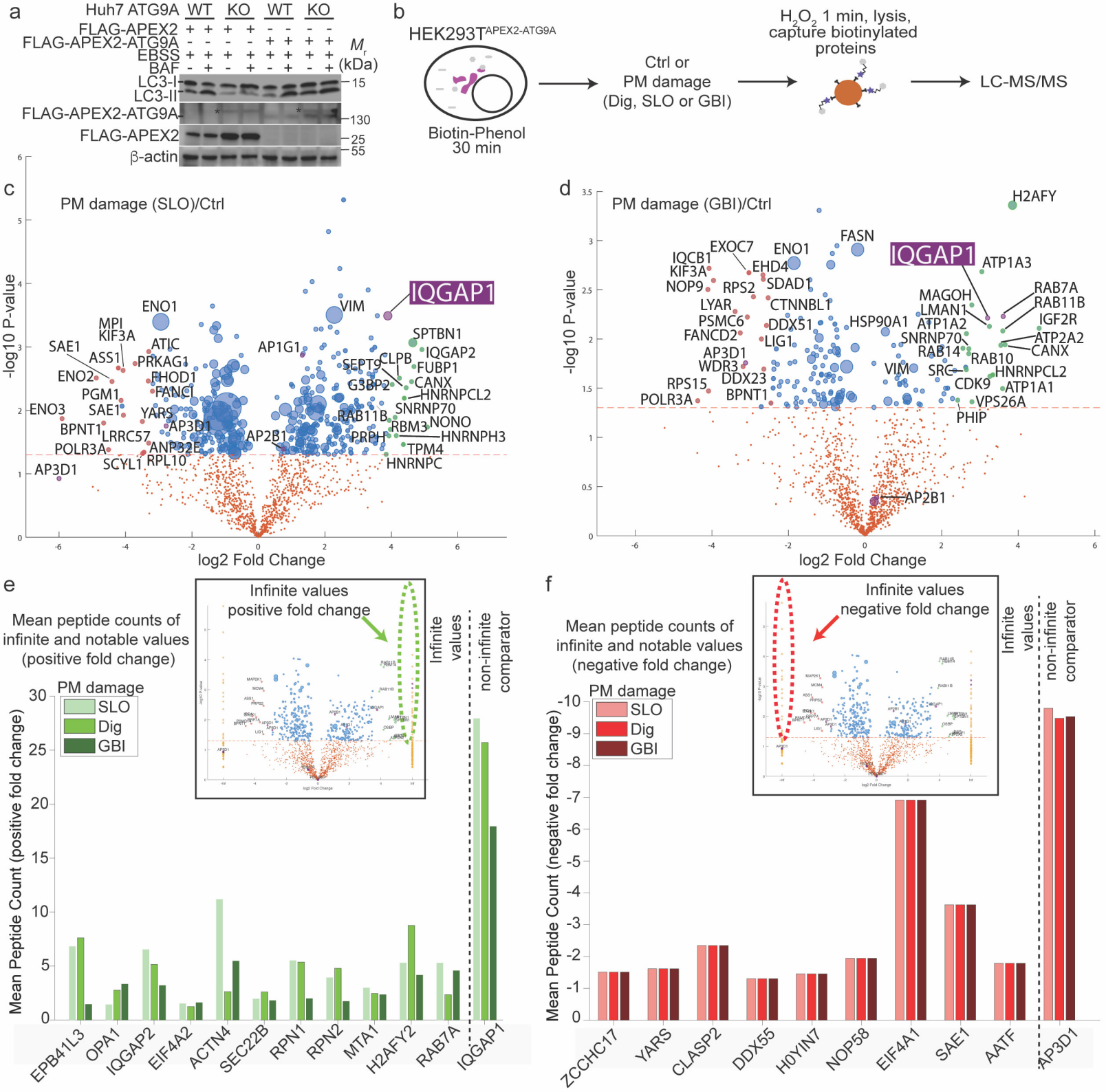

Ext Data Fig6

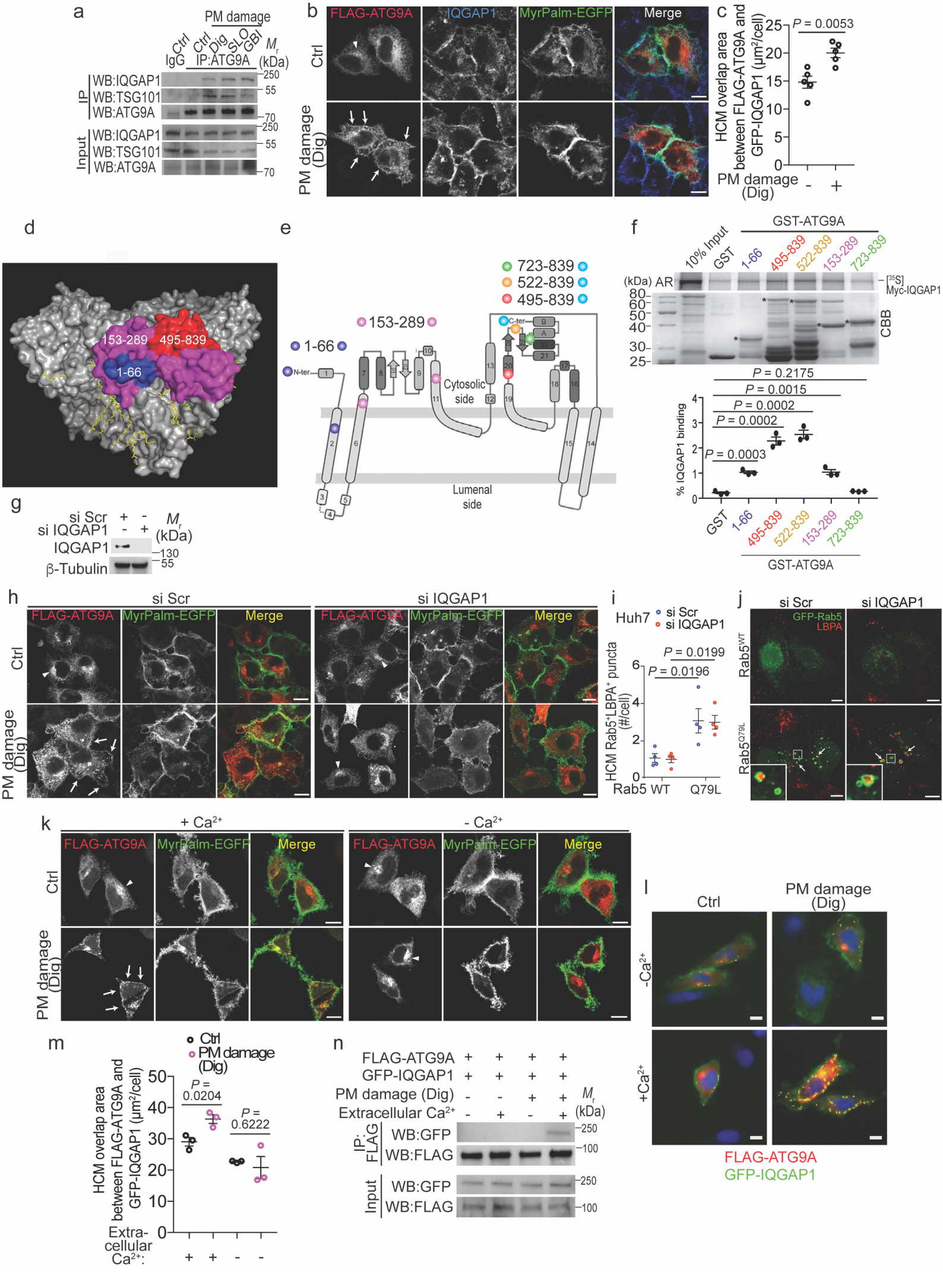

Ext Data Fig7

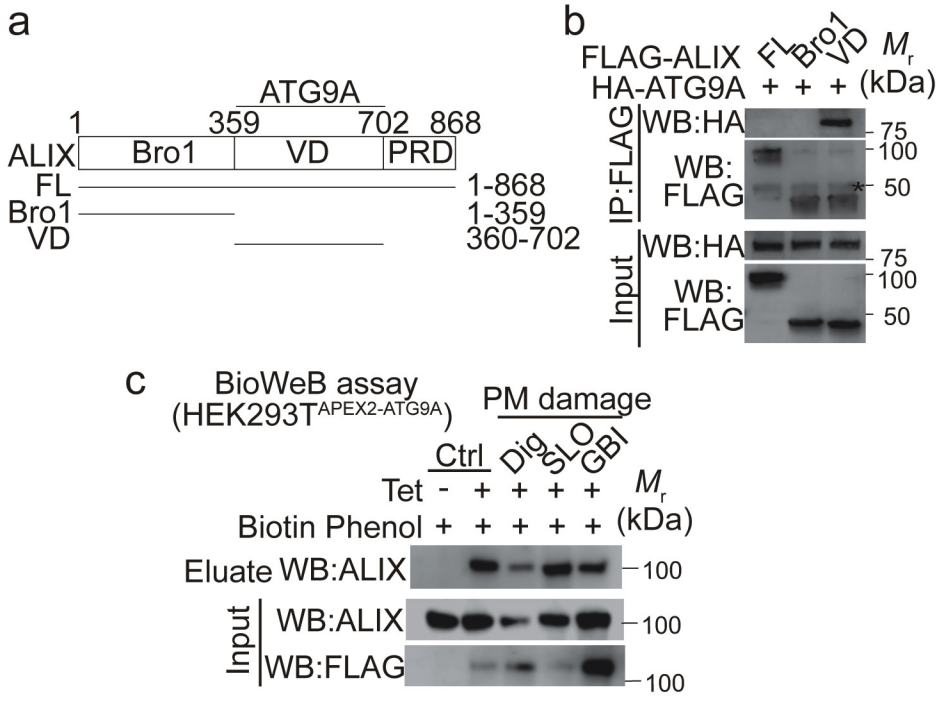

Ext Data Fig8

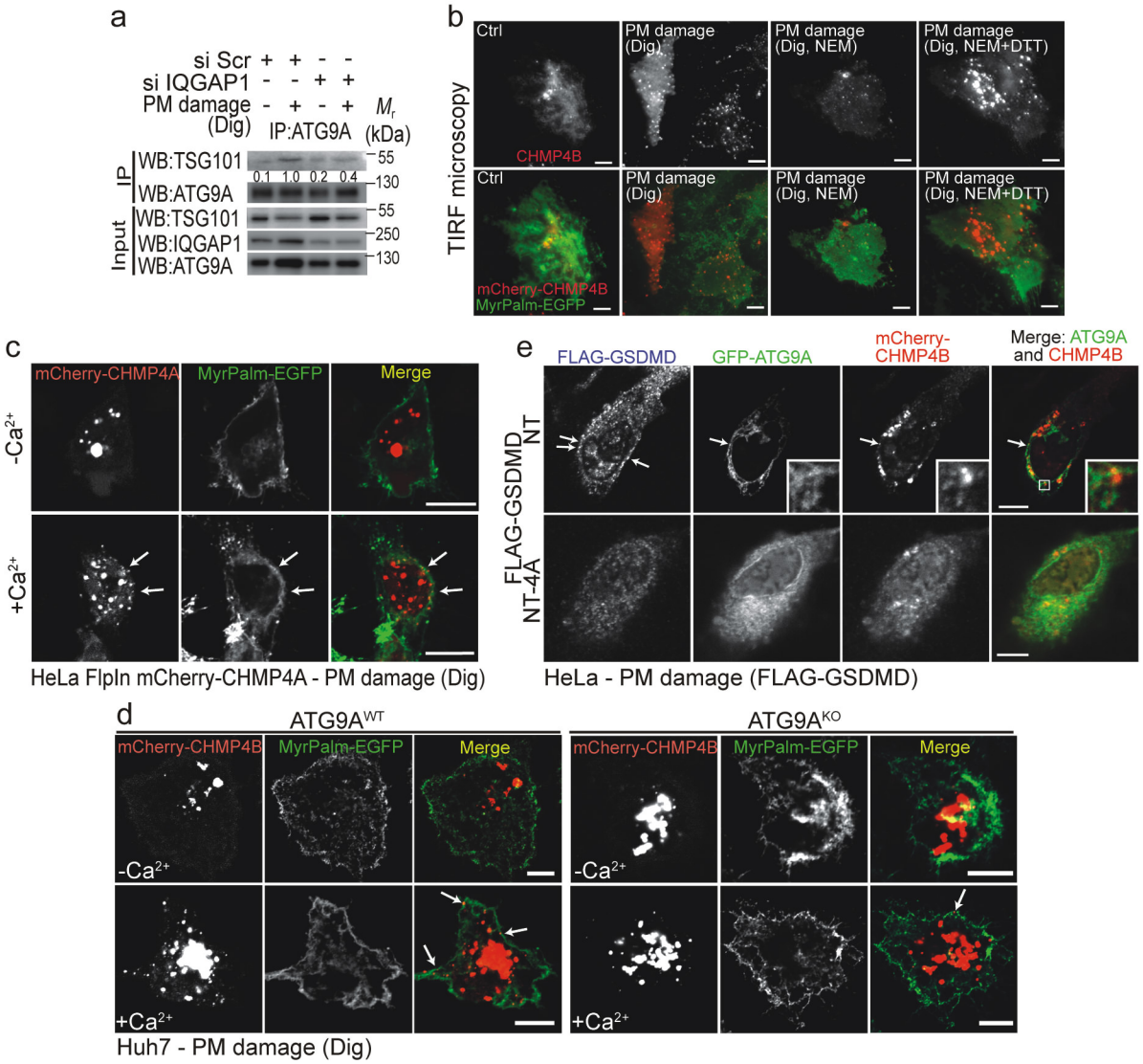

Ext Data Fig9

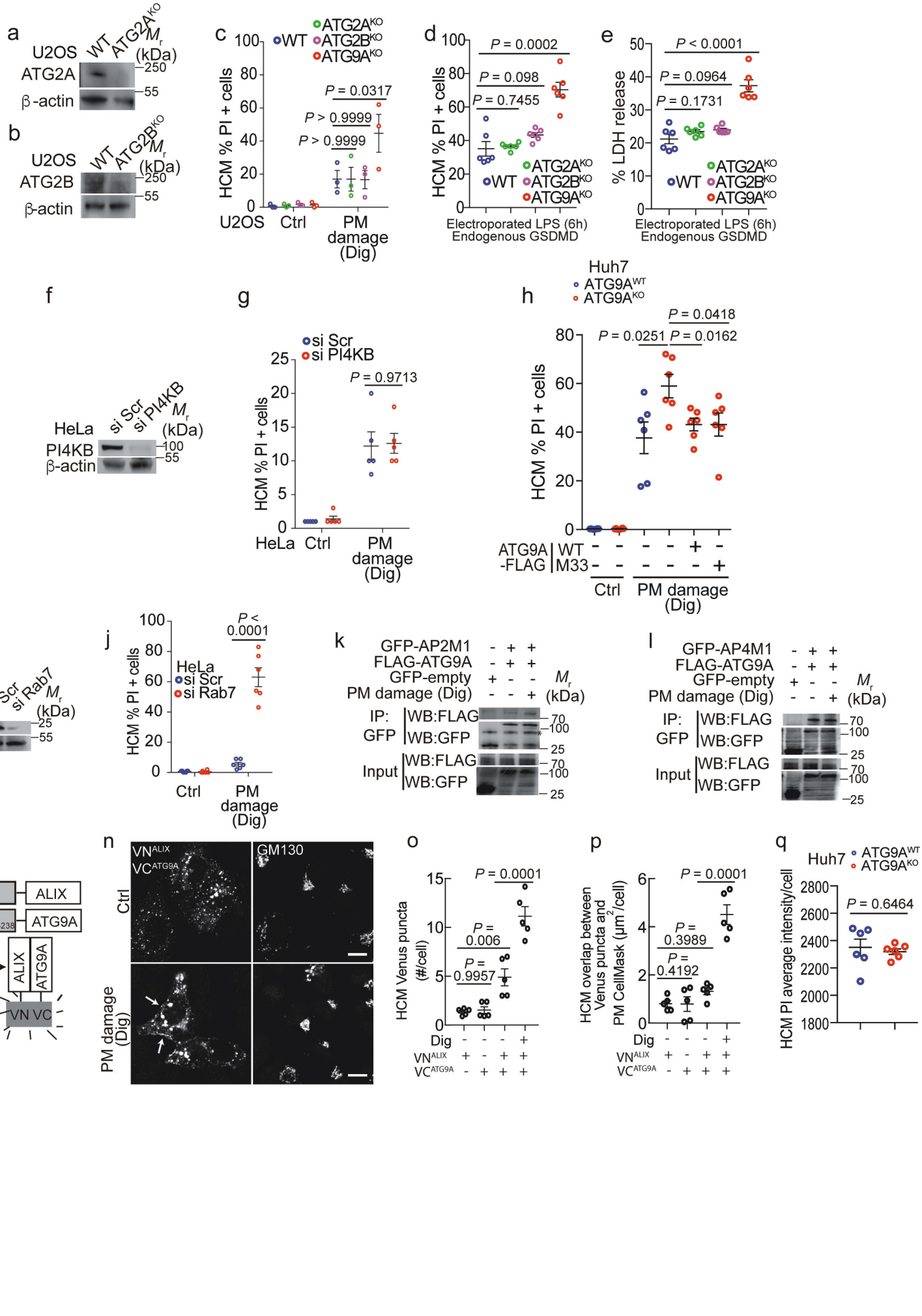

Ext Data Fig10